AD-A140 167 JOURNAL OF AERONAUTICAL MATERIALS (SELECTED ARTICLES) 1/1
(U) FOREIGN TECHNOLOGY DIV WRIGHT-PATTERSON AFB OH
R WANG ET AL. 27 MAR 84 FTD-ID(RS)T-1869-83

UNCLASSIFIED F/G 11/6 NL

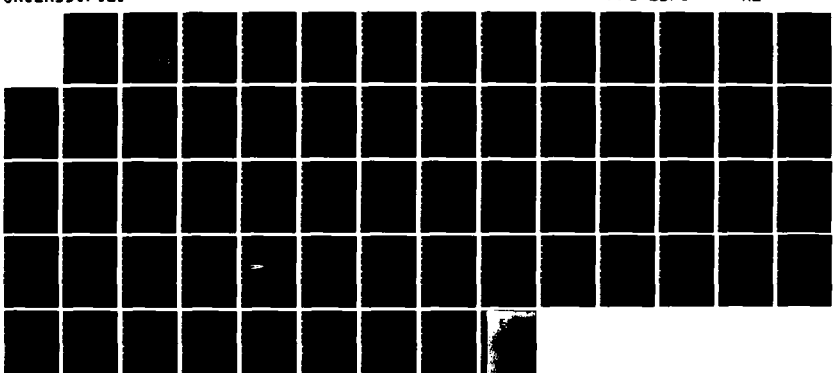

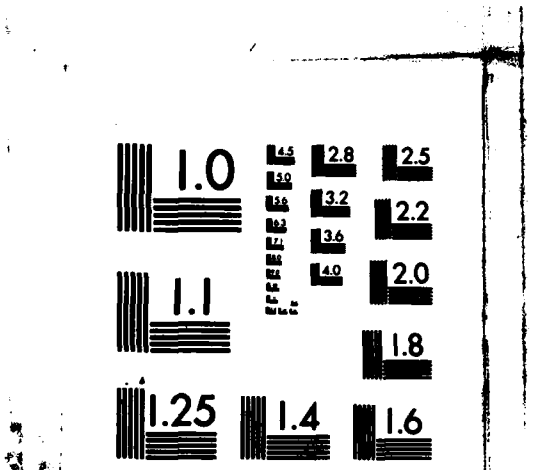

MICROCOPY RESOLUTION TEST CHART
NATIONAL BUREAU OF STANDARDS-1963-A

(2)

FTD-ID(RS)T-1869-83

AD A140167

FOREIGN TECHNOLOGY DIVISION

JOURNAL OF AERONAUTICAL MATERIALS
(Selected Articles)

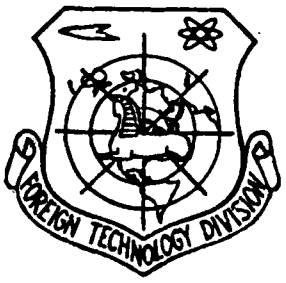

DTIC
ELECTE
APR 17 1984
S D
B

DTIC FILE COPY

Approved for public release;
distribution unlimited.

84 04 16 168

EDITED TRANSLATION

FTD-ID(RS)T-1869-83 27 March 1984

MICROFICHE NR: FTD-84-C-000314

JOURNAL OF AERONAUTICAL MATERIALS (Selected articles)

English pages: 58

Source: Hangkong Cailiao, Vol. 2, Nr. 1, pp. 1-6; 19-24; 25-31; 40-46; 47-52;

Country of origin: China
Translated by: LEO KANNER ASSOCIATES
F33657-81-D0264
Requester: FTD/TQTA
Approved for public release; distribution unlimited.

THIS TRANSLATION IS A RENDITION OF THE ORIGINAL FOREIGN TEXT WITHOUT ANY ANALYTICAL OR EDITORIAL COMMENT. STATEMENTS OR THEORIES ADVOCATED OR IMPLIED ARE THOSE OF THE SOURCE AND DO NOT NECESSARILY REFLECT THE POSITION OR OPINION OF THE FOREIGN TECHNOLOGY DIVISION.

PREPARED BY:

TRANSLATION DIVISION
FOREIGN TECHNOLOGY DIVISION
WP-AFB, OHIO.

GRAPHICS DISCLAIMER

All figures, graphics, tables, equations, etc. merged into this translation were extracted from the best quality copy available.

Accession For	
NTIS GRA&I	☑
DTIC TAB	☐
Unannounced	☐
Justification	
By	
Distribution/	
Availability Codes	
Dist	Avail and/or Special
A-1	

DTIC COPY INSPECTED

TABLE OF CONTENTS Page

STRESS CORROSION CRACKING OF METASTABLE AUSTENITIC STAINLESS STEEL ----------1

RESEARCH ON WAVE GRAIN BOUNDARY HEAT TREATMENT PROCESSES FOR GH220 ALLOY----------11

EFFECT OF HEAT TREATMENT ON FINE STRUCTURE AND MECHANICAL PROPERTIES IN ULTRAHIGH STRENGTH STEELS----------22

STUDY OF THE FRACTURE TOUGHNESS OF AIRCRAFT ACRYLIC SHEETS-----34

STUDY OF UNIAXIAL COMPRESSIVE STABILITY OF CARBON FIBER COMPOSITE STIFFENED PLATES----------47

STRESS CORROSION CRACKING OF METASTABLE AUSTENITIC STAINLESS STEEL

Wang Renzhi, Li Xiangbin, Yin Yuanfa and Yan Minggao

The stress corrosion cracking of metastable austenitic stainless steel has been investigated. The following results are obtained, (1) The plastic induced phase transformation $\gamma \rightarrow \alpha'$ occurs in the plastic zone ahead of crack tip. Thus the shallow layer of fracture surface consists of α' phase. (2) SCC for such metastable austenitic stainless steel is, as matter of fact, a cleavage-like fracture. The crack propagation and the fracture process are as follows.

$$\gamma\,(\text{fcc}) \xrightarrow{\text{plastic deformation}} \alpha'\,(\text{bcc}) \xrightarrow{\text{anodic solution}} \text{cleavage-like fracture}$$

I. Introductory

Generally, the stress corrosion cracking (SCC) of metastable austenite (gamma) stainless steel does not induce $\gamma \rightarrow \alpha'$ transformation; however, owing to diffusion and aggregation of hydrogen atoms at the crack tip and its plastic strain, the SCC of metastable gamma phase stainless steel (18Cr-8Ni) can cause different degree of $\gamma \rightarrow \alpha'$ transformation [1-4] at the crack tip. As pointed out in recent studies, no $\gamma \rightarrow \alpha'$ transformation [5] occurs in the stress-corrosion crack-tip zone of this type of steel. Some other researchers pointed out [1, 6] that the crack extends along the lath of the formed α' phase, and often a clear cleavage-like crack appears [3, 7-9] at the crack tip following fracture. However,

most of past research used an electron diffraction technique to determine the α' phase and its content at the SCC tip or its plastic zone. Obviously, on one hand this testing technique is limited by measurement accuracy; on the other hand inaccurate or even entirely opposite results may be obtained due to improper selection of the electron diffraction zone. In addition, until now very few manuscripts have studied the relations between the formation of the α' phase at the SCC tip and the mode of cleavage fracture. Therefore, this paper utilizes the x-ray diffraction analysis method mainly to study the formation of the α' phase and its transformation quantity at the SCC tip; also studied are relations between the α' phase and the fracture mode.

II. Test Methods

This test uses 1Cr18Ni9Ti metastable gamma phase stainless steel; its chemical composition, mechanical properties, and heat treatment process are listed in Table 1. A 2-mm thick rolled lath was machined into a three-point bending stress corrosion test specimen with dimensions of 100x10x1.5 mm. The corrosion solution is 5N H_2SO_4 + 0.5N NaCl, and the testing temperature is room temperature. Bending was applied to the specimen and then it was soaked into a solution until broken.

Table 1. Heat treatment, chemical composition and mechanical properties of 1Cr18Ni9Ti steel.

(1) 热处理	(2) 化学成分，%								(3) 力学性能			
	C	Mn	Si	P	S	Cr	Ni	Ti	E kg/mm²	σ_b kg/mm²	$\sigma_{0.2}$ kg/mm²	δ %
1050°C(水冷)(4)	0.06	0.54	0.73	0.029	0.06	18.1	9.10	0.50	19000	60	25	~50

Key: (1) Heat treatment; (2) Chemical composition; (3) Mechanical properties; (4) Water cooling.

On a 2903 model x-ray diffraction instrument, CrKα radiation was used to record a curve pattern of the diffraction spectrum; some curve patterns were recorded on a RU200 diffraction instrument. Based on integration intensity of the (220) spectral curve of the gamma phase and the (211) spectral curve of the α' phase, the content of α' was calculated. By using a JSM-35 model scanning electron microscope and a JEM-200A model transmission electron microscope, the crack appearance and structural texture were observed.

The cathode hydrogen-filling solution of the test specimen is 4 percent H_2SO_4 + 0.2N $NaAsO_2$. The current density is 0.5 mA/cm^2 and carbon electrodes were used.

III. Test Results

3.1. Plastic strain-induced $\gamma \rightarrow \alpha'$ transformation

Strengthening with surface spraying of tiny spherules causes cyclic plastic strain [10] of surface-layer metal; the plastic strain can cause $\gamma \rightarrow \alpha'$ transformation of metastable gamma phase steel. The surface spraying of tiny spherules can gradually reduce the strain amount of the surface-layer metal with increase of surface-layer depth; therefore, the amount of α' phase also decreases with depth b (Fig. 1). If the test specimen (after spraying with tiny spherules) passes through different degrees of small elongation strain, the transformation amount of the α' phase has a matrix anomaly ($\Delta a/a$) and dimensions (D) of sub-crystal grains that vary with the amount of strain. This variation of structural texture can be revealed with variation of the integration width of the (211) spectral curve of the α' phase. As revealed by the shape of the β-δ curve in Fig. 1, with a decrease of strain amount (i.e., with increase of depth of surface layer), the $\Delta a/a$ of the α' phase gradually decreases and D gradually increases.

Figures 2 and 3 (refer to plate 1 [not available in the xerox copies of text]) show the appearance of the α' phase in the lath and electron diffraction patterns after transformation of the gamma phase. The measurement results of the gamma and α' phases are: for gamma phase, HV=275; and for α' phase, HV=460.

Following the elongation fracture of the test specimen at room temperature, the amount of α' phase of various portions measured, and the amount of α' phase at the lateral side close to the terminal of the shrunk neck are both at 50 percent; however, only in the high strain zone at the surface of the shrunk-neck crack is the amount of α' phase 100 percent. The integration width is β=4.45° for the (211) spectral curve of this portion.

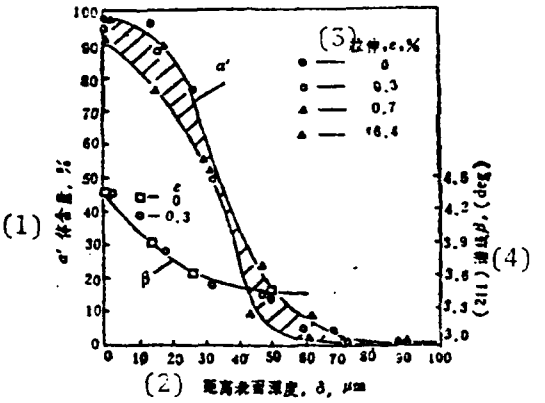

Fig. 1. Plastic strain of the surface layer of 1Cr18Ni9Ti steel, the later elongation strain-induced amount of the α' phase, and the variation of the (211) spectral curve β along the depth δ.
Key: (1) Content of α' phase; (2) Distance of depth from the surface layer; (3) Elongation; (4) (211) spectral curve .

3.2. Cathode hydrogen-filling-induced γ->α' transformation

Figure 4 shows the patterns and positions of (111) and (311) spectral curves of the gamma phase before and after cathode hydrogen filling (5 hours) of 1Cr18Ni9Ti steel. Hydrogen infiltration causes the decrease of the angle of the gamma phase and the diffraction angle (2θ) of a high inclination spectral curve, and the widening of the β value of the spectral curve. These variations explain that hydrogen atoms can expand the crystal lattice of the gamma phase and increase Δa/a.

3.3. α' phase at stress corrosion crack

Figure 5 shows patterns of x-ray diffraction spectral curves of gamma and α' phases at different depths of the SCC tip. When the electrolytic buffing method is used to remove the crack surface δ about 1μm deep, the α' phase disappears generally. Based on the penetration depth (approximately 11 μm) of CrK_α radiation

in steel, by using $I_{(211)\alpha'}$ and $I_{(220)\gamma}$ of the surface of the SCC tip, the calculated α' content is greater than or equal to 90 percent, distributed in the surface layer $\leq 1\mu m$ deep.

The beta (β) value of the (220) spectral curve of the gamma phase becomes narrowed with an increase in depth into the surface layer. β (=4.5°) of the α' phase at surface of the SCC tip; the value of β is entirely consistent with the value at the surface of the plastic strain (with spraying of tiny spherules) and at the crack surface of the shrunk neck due to elongation fracture.

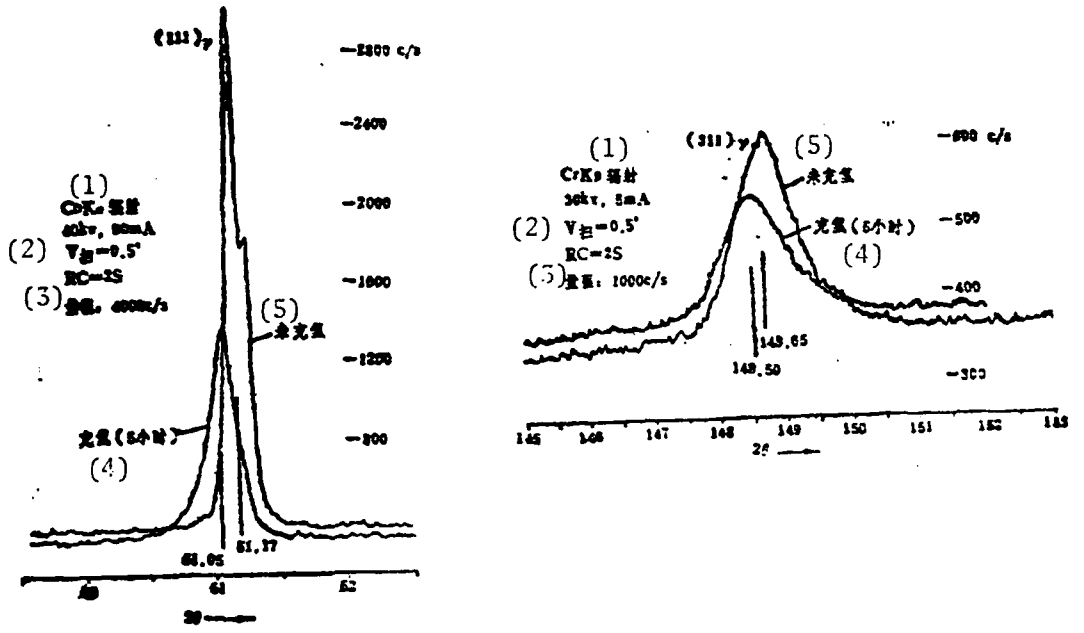

Fig. 4. Patterns of (111) (CoK_α radiation) and (311) (CrK_α radiation) spectral curves of the gamma phase before and after hydrogen filling (5 hours) of a cathode of 1Cr18Ni9Ti steel.
Key: (1) Radiation; (2) Scanning; (3) Measurement range; (4) Hydrogen filling (five hours); (5) Without hydrogen filling.

3.4. Observation of stress corrosion crack

Figure 6 (refer to plate 1 [not included in the xerox copies of text]) shows the appearance of stress corrosion crack patterns at the lateral side of the test specimen; the crack extends by penetrating the crystals. Figure 7 (refer

to plate 2 [not available in xerox copies of text]) shows the diagram from the scanning electron microscope with the appearance of the SCC tip. All fractures are brittle fractures penetrating crystals while cracks appearing in a feather pattern, cleavage river pattern, cleavage terrace pattern, and sector pattern. In some zones, a tunnel pattern appears as the crack source.

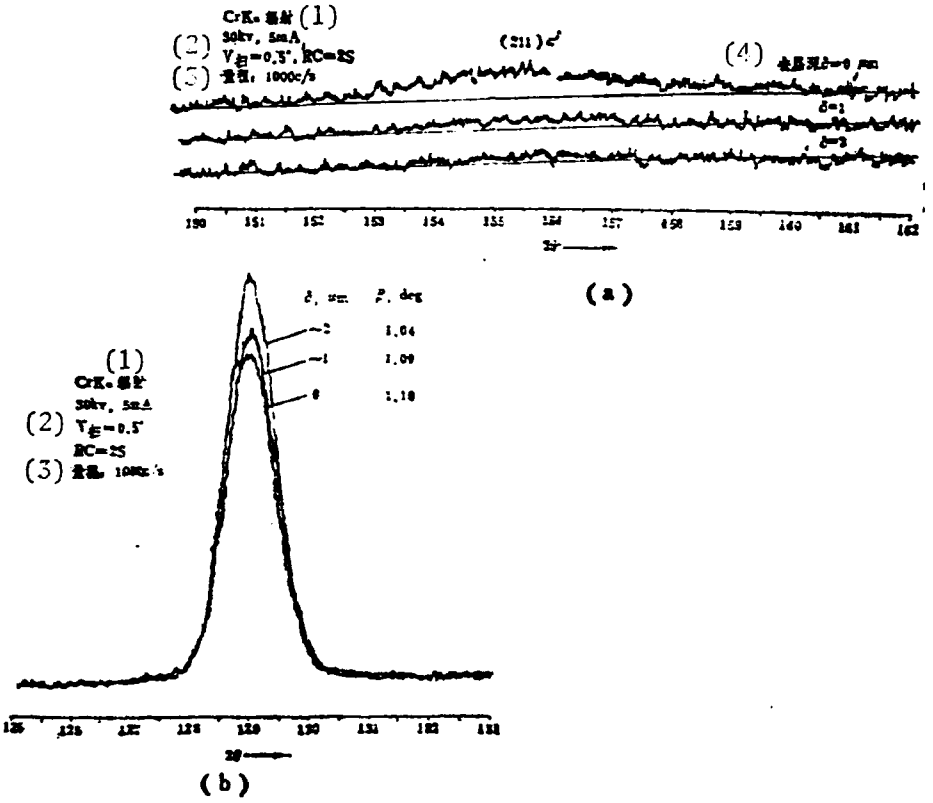

Fig. 5. Patterns of $(211)_\alpha$, (a) and $(220)_\gamma$ (b) spectral curves (CrK_α radiation) on δ of the surface and different depths of SCC (fracture time: 480 hours) tip of 1Cr18Ni9Ti steel.
Key: (1) Radiation; (2) Scanning; (3) Measurement range; (4) Removal of layer to a depth.

IV. Discussion

The plastic strain at room temperature can cause $\gamma \rightarrow \alpha'$ transformation of the metastable gamma phase (Fig. 1). The amount of newly formed α' phase is

determined by the plastic strain quantity ε. In addition, only when ε attains a sufficiently high value can this $\gamma \rightarrow \alpha'$ transformation be completed. As revealed by the degree of $\gamma \rightarrow \alpha'$ transformation of various portions of the test specimen with elongation fracture at room temperature, only in the high strain zone at the crack surface of the shrunk neck can the $\gamma \rightarrow \alpha'$ transformation be completed.

Cathode filling of hydrogen can expand the crystal lattices of the γ phase (Fig. 4). Besides, Holzworth [4] discovered that hydrogen filling can have $\gamma \rightarrow \alpha'$ and $\gamma \rightarrow \varepsilon$ transformations in 304 stainless steel. However, even under the condition of relatively sufficient hydrogen filling at the cathode, only small portions of the gamma phase can have the aforementioned transformation.

As revealed by x-ray analysis at the SCC crack surface, the gamma phase within ($\lesssim$1 μm) a thin layer of the crack surface is basically transformed into the α' phase (90 percent). Besides, the beta values of (211) spectral curves of the α' phase at the crack surface, and the beta value at a high strain zone of elongation fracture, and plastic strain of tiny spherule spraying are equal to one another ($\beta \sim 4.4°$). Obviously, the $\gamma \rightarrow \alpha'$ transformation at the SCC tip is mainly caused by plastic strain of the crack tip zone. Nakayama [5] observed under a high energy transmission electron microscope that there is a tiny plastic strain zone at the stress corrosion crack tip of 304 steel. However, the Japanese researcher used an electrolytic buffing method to thin the stress corrosion test specimen for the electron microscope. As the α' phase newly formed at crack tip is very thin (2 m), in the thinning process the α' phase may be dissolved; in addition to improper selection of diffraction zone, it is possible that no α' phase is discovered at the crack tip zone.

The beta value of the (220) spectral curve of the gamma phase at the SCC surface becomes gradually thinner when deeper from the surface layer, decreasing from $\beta = 1.1°$ at the crack surface to $\beta = 1.04°$ ($\delta \gtrsim 2\mu m$) (Fig. 5). The widening of the beta value at the SCC surface is possibly the result of plastic strain, infiltration of hydrogen atoms in the solution, or the combined function of the two aforementioned causes.

All SCC fractures are brittle fractures; the crack is originated inside crystal grains and extends by penetrating the crystal grains (Fig. 6 [Fig. 6 is

not included in the xerox copies of text]). There are tunnel patterns (Fig. 7, a [Fig. 7 is not included in the xerox copies of text]) as observed by Scully [7]. However, the further expansion of the crack proceeds in the cleavage fracture form (Fig. 7, b, c and d); even the sector pattern is one form of cleavage-like fractures (Fig. 6, e).

It is generally considered that no cleavage fracture occurs on the gamma phase of the face centered cube (fcc); even for elongation fracture at low temperature (-196°C), the crack is of the selector-wave pattern [1] though the α' phase forms at the crack, which is caused by ductile fracture. However, in the SCC process, it can be determined from the existence of large α' phase contents (greater than or equal to 90 percent) at the crack that the crack extends along the newly formed α' phase lath. Nakayama [5] and Li Minzhi [9] used the analysis method of corrosion pits at the crack surface; both discovered that the SCC tip of this type of steel is mainly on the (100) and (110) faces, not the (111) face. It is known from test results in this paper that this is not gamma phase, but the (100) and (110) faces of the α' phase. However, (100) is just the cleavage face of the body centered cube (bcc) metal. Hence, the SCC of this type metastable gamma phase stainless steel is actually the fracture phenomenon controlled by the cleavage-like fracture regime of α' phase (bcc).

Concerning the crack extension due to stress corrosion, Birley [1] considered that this may be related to dissolving the α' phase at the crack tip. However, this dissolving procedure is also related to the electrolytic potential difference between gamma and α'. This test determined the gamma phase and dulling current density I_p (at the 500 mV dulling potential on an identical solution) of the α' phase induced by plastic strain; for the gamma phase, I_p=12∿17 $\mu A/cm^2$, and for the α' phase, I=30∿50 $\mu A/cm^2$. Obviously, under the same corrosion conditions, the α' phase has a higher electrolytic dissolving rate than the gamma phase; therefore, the crack can predominantly extend along the newly formed α' phase lath. The strain α' phase has a higher dislocation density (when comparing Figs. 3 and 4) than the gamma phase. This is also one of the important causes determining that the α' phase has a high capability of electrolytic dissolving. Reed revealed [11], based on research on transformation on the α' phase in 18-8 steel, that the inertial precipitation face of the α' phase is $(111)_\gamma$; however, the orientation relations between α' and gamma still abide by the relation equation

(of Kurdjumov and Sachs): $(111)_{\gamma}//(101)_{\alpha'}$. From the aforementioned, Fig. 8 can illustrate the SCC extension regime with the dislocation model: the plastic strain of the crack tip induces slip of (111) in the gamma phase, thus forming the strain α' phase; the dislocation moves on the $(110)_{\alpha'}$ face along the [111] direction, resulting in forming considerable crowding (Fig. 8, a) at the crack tip; the α' phase (with high dislocation density) of the crack tip comes into contact with the solution to form a dissolving anode, thus releasing the crowded dislocation (Fig. 8, b). Repeating the aforementioned process, the crack has a cleavage-like fracture (Fig. 8, c) along the macroscopic $(100)_{\alpha'}$ face. Similarly, by using this model, the cleavage-like fracture regime along the $(110)_{\alpha'}$ face can be explained.

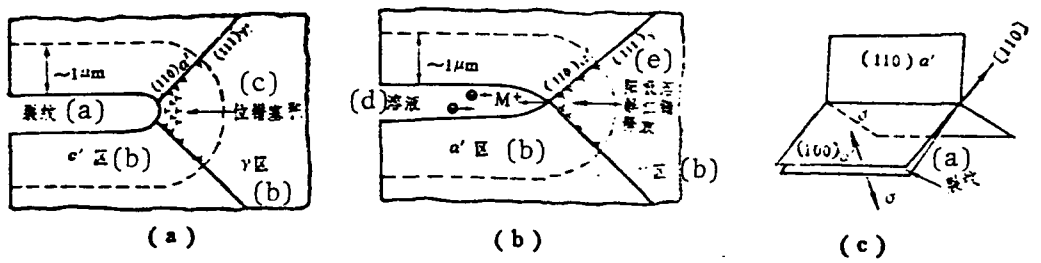

Fig. 8. Dislocation models of cleavage-like fracture of SCC of metastable gamma phase stainless steel: (a) dislocation crowding of α' phase at crack tip before anode dissolves; (b) dislocation release at crack tip after anode dissolves; and (c) dislocation model of cleavage fracture of crack tip along $(100)_{\alpha'}$.
Key: (a) Crack; (b) Zone; (c) Dislocation crowding; (d) Solution; (e) Dislocation release following anode dissolving.

According to the aforementioned descriptions, the extension and fracture process of a stress corrosion crack of metastable gamma phase stainless steel can be summarized as follows:

$$\gamma(\text{fcc}) \xrightarrow{\text{plastic strain}} \alpha'(\text{bcc}) \xrightarrow{\text{anode dissolving of plastic strain}} \text{cleavage-like fracture along the macroscopic (100) face.}$$

V. Conclusion

After studying strain in the crack tip plastic zone due to stress corrosion induced $\gamma \rightarrow \alpha'$ transformation; the SCC crack surface is mainly the (bcc) of the α' phase.

2. The anode dissolving of the high dislocation density α' phase at the crack tip causes continuous extension of the crack along the newly formed strain α' phase lath.

3. The SCC regime of this type metastable gamma phase steel is actually the cleavage-like fracture of the α' phase. The extension and cracking process of the fracture is:

$$\gamma(\text{fcc}) \xrightarrow{\text{plastic strain}} \alpha' \text{ (bcc)} \xrightarrow{\text{dissolving of anode}} \text{cleavage-like fracture.}$$

LITERATURE

[1] Birley, S.S., Tromans, D., Corrosion, 27(1971)2, 63.

[2] Nelson, J.L., Beavers, J.A., Metall. Trans., 10A(1979), 658.

[3] Liu, R., Narita, N., Altstetler, C., Birnbaum, H., Pugh, E.N., Metall. Trans., 11A(1980)9, 1563.

[4] Holzworth, M.L., Louthan, M.R., Jr., Corrosion, 24(1968)4, 110.

[5] Nakayama, T., Takano, M., Corrosion, 37(1981)4, 226.

[6] Edeleanu, C., Stress Corrosion Cracking and Embrittlement, John Wiley and Sons, New York, 1956, 135.

[7] Scully, C.J., The Theory of Stress Corrosion Cracking in Alloys, NATO, 1971, 127—166.

8. Xue Enchen, Peng Rihui, Lu Zhengliang, Liu Tingcai, Hu Mingcuo, and He Mingshan, JIXIE GONGCHENG CAILIAO [MATERIALS FOR MECHANICAL ENGINEERING], 5 (1981) 1, 48.

9. Li Minzhi and Lu Zhengliang, Analysis of Crack Forms and Corrosion Pits due to Stress Corrosion of Austenite, General Iron and Steel Research Institute, Ministry of Metallurgy Industry, 1980, Summary of Papers Presented at Annual Science Conference (Part I), 84.

[10] Wang Renzhi, Li Xiangbin, Tan Yonggui, Yan Minggao, Proceedings of First International Conference on Shot-Peening, Paris, 1981.

[11] Reed, R.P., Acta Metall., 10(1962)9, 865.

RESEARCH ON WAVE GRAIN BOUNDARY HEAT TREATMENT PROCESSES FOR GH220 ALLOY

Tan Jufen, Jiang Shurong, and Tian Shifan*

In this paper, the changes of grain boundaries and grain structures of GH220 alloy during cooling with various cooling rates after solution treatment and their effects on the mechanical properties of this alloy were investigated. It was shown that wave grain boundaries can be obtained by the "slow cooling", "isothemal-quenching" and "slow cooling plus re-solution" heat treatments and that a suitable combination of wave grain boundaries and desirable matrix structures would be quite beneficial to improve both creep-rupture strength and ductility and thus to obtain good overall properties. It is recommended that there are two heat treatment processes which appear to be better than the "standard procedure" for GH220 alloy."

I. Foreword

The GH220 alloy is a highly alloyed nickel-base transformed high-temperature alloy; its use temperature can be as high as 950°C.

A rational heat treatment process is very important to exploit the alloy's potential and to enhance its comprehensive properties. The purpose of this paper is to present better heat-treatment processes by studying the effect on the

* Xu Shibin and Yang Yurong also took part in the work.

intracrystal grain structure and its properties of alloy crystal boundaries of various heat-treatment processes.

There were studies earlier concerning the formation and function of wave grain boundaries in high-temperature alloys. As reported by some papers [1-5], the wave crystal boundaries are effective in enhancing strength and preventing fracture of grain boundaries. As revealed by some other researchers [6-9], though some heat-treatment processes can lead to wave grain boundaries, yet only plasticity is enhanced while persistent strength is lowered. Some work in the past only paid attention to ways of obtaining wave grain boundaries but neglected the fact that the heat-treatment process has a similar important function on grain structure; therefore, the results were not very good. This work pays attention to the dual influence on grain boundaries and structure of the heat-treatment process. The coordination of grain boundaries and intracrystal strength can attain a better result. It is presented that the heat-treatment setup can attain better crystal structure and enhance strength and plasticity.

II. Materials and Testing Processes

The test specimens are ϕ32 mm GH220 rod materials; the specimens were smelted with a duplex process of vacuum induction and vacuum self-consumption, and rolled while wrapped in a sleeve. The nominal composition (weight percentages) of the material is: C 0.05, Cr 10.0, Co 15.0, Mo 5.5, W 5.5, Al 4.1, Ti 2.4 and V 0.30.

Table 1 lists the test process. The T0 process is the original standard heat-treatment process as the comparison basis of various processes. In other processes, the solid-solution treatment temperature, time-effect treatment temperature, and time are the same as the standard heat-treatment process; however, changes have been made in the cooling rate following solid-solution treatment, temperature and time of isothermal treatment, temperature of secondary treatment, and addition of a work step for the remelting treatment.

Tests on all mechanical properties proceeded according to the standard test method for aviation materials. Optical microscopes and transmission electron microscopes are used to observe the metallographic structure, and scanning electron microscopes are used to observe cracks.

Table 1. Heat-treatment test processes.

代号 (1)	固溶处理 (2)	冷速 (3)	等温或二次处理 (4)（空冷）	回溶处理 (5)（空冷）	时效处理 (6)（空冷）
T0	1220°C/4小时 (7)	空冷到室温 (8)	1050°C/4小时 (7)	—	950°C/2小时 (7)
T1		1°C/分 (9)	1050°C/4小时 (7)	—	
T2		3°C/分 (9)		—	
T3		5°C/分 (9)		—	
T4		随炉 (10)		—	
T5		转炉 (11)	1050°C/4小时 (7)	—	
T6			1075°C/4小时 (7)	—	
T7			1100°C/4小时 (7)	—	
T8			1125°C/4小时 (7)	—	
T9			1100°C/2小时 (7)	—	
T10			1100°C/6小时 (7)	—	
T11		随炉 (10)	1050°C/4小时 (7)	1100°C/4小时 (7)	
T12				1125°C/4小时 (7)	
T13		空冷到室温 (8)	1075°C/4小时 (7)	—	
T14			1100°C/4小时 (7)	—	
T15			1125°C/4小时 (7)	—	

Key: (1) Process code; (2) Solid-solution treatment; (3) Cooling rate; (4) Isothermal or secondary treatment (air cooling); (5) Remelting treatment (air cooling); (6) Time-effect treatment (air cooling); (7) Hours; (8) To room temperature with air cooling; (9) Minute; (10) Cooling with furnace; (11) Rotary furnace.

III. Test Results and Discussion

3.1. Matching between strength of grain boundaries and intracrystal strength

The T0 and T13∿T15 processes are air-cooling heat-treatment processes. After treatment with the T0 process, grain boundaries are level and straight; the intracrystal γ' phase is of square shape with orderly arrangement (Fig. 1a, refer to plate no. 9 [not available in xerox copies of text]). After treatment with T13∿T15 processes, grain boundaries are also level and straight; however, in the vicinity of the grain boundaries there is large γ' phase zone; two kinds

of dimensions of the γ' phase appear within the crystals (Fig. 1b, refer to plate no. 9). One type is those precipitated during air cooling after solid-solution treatment and the growth of a large γ' phase during secondary treatment. Another type is those precipitated during air cooling after secondary treatment with growth of a small γ' phase during time-effect treatment. From Fig. 2, following the air-cooling treatment generally hardness (intracrystal strength) is higher but the persistent strength is not high, and the persistent plasticity is very low.

T1∿T4 are slow-cooling heat-treatment processes; the slow-cooling rates are, respectively, 1, 3, and 5°C per minute and cooling within the furnace. After slow-cooling treatment, the grain boundaries are obviously wavy (Fig. 1c, refer to plate no. 9), and the large intracrystal γ' phase is scattered in diffusion; there is growth during precipitation and during the time effect of air cooling after secondary treatment. After slow-cooling treatment, the alloy hardness is reduced; its persistent strength is also slightly reduced, but the persistent plasticity is apparently enhanced. The mean ductility index is 9.8 percent, corresponding to 2.7 times that of the T0 process. By comparing the T1, T2, T3 and T5 processes (Fig. 3), we can see that with increasing slow-cooling rate, the persistent strength is slightly enhanced while plasticity is slightly reduced. However, when the cooling rate is as high as that of the air-cooling process (T0 process), although hardness is enhanced, persistent strength and plasticity decrease.

T5∿T10 processes are isothermal heat-treatment processes, from one solid-solution treatment to directly turning to a lower temperature for isothermal treatment. After isothermal treatment, the grain boundaries are wavy and degree of waviness is smaller (Fig. 1d, refer to plate no. 9). There are γ' phases within crystals with two types of dimensions, similar to the appearance after slow cooling but relatively more homogeneous than for slow cooling. The isothermal treatment can enhance the persistent strength, and apparently enhance the persistent plasticity (Fig. 4). The time of isothermal treatment has no apparent effect on the properties (Fig. 4, T7, T9 and T10). In this type of processes, T7 is better.

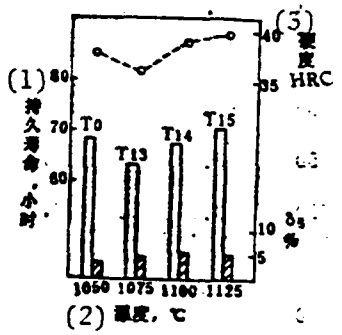

Fig. 2. Hardness and (940°C) persistent properties* after air-cooling treatment.
Key: (1) Persistent service life, hours; (2) Temperature; (3) Hardness.

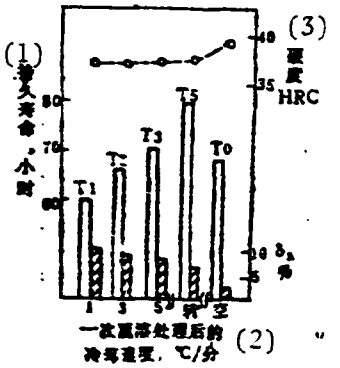

Fig. 3. Effect on hardness and (940°C) persistent properties of cooling rate of solid-solution treatment.
Key: (1) Persistent service life, hours; (2) Cooling rate (°C/min) after one remelting treatment; (3) Hardness.

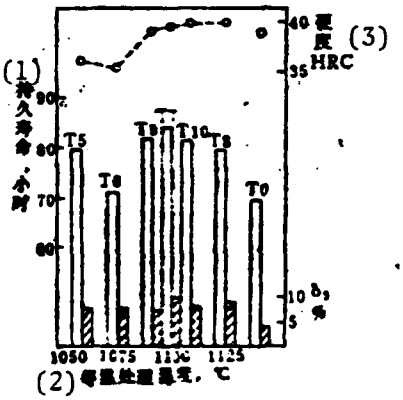

Fig. 4. Hardness and (940°C) persistent properties after isothermal treatment.
Key: (1) Persistent service life, hours; (2) Temperautre of isothermal treatment; (3) Hardness.

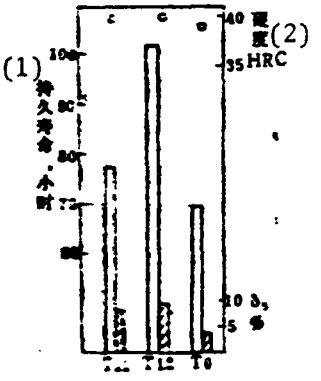

Fig. 5. Hardness and (940°C) persistent properties after slow cooling and remelting treatment.
Key: (1) Persistent service life, hours; (2) Hardness.

* All persistent (test) stresses are 22 kg/mm^2 in Figs. 2 through 5.

T11 and T12 processes are slow-cooling and remelting heat-treatment processes. After T11 and T12 processes of treatment, the situation of the grain boundaries is similar to that following slow cooling. Owing to remelting treatment, the intracrystal structure has changed. During remelting treatment, one part of the original intracrystal γ' phase is dissolved in a solid-solution. In the later work steps, a very small γ' phase is again precipitated. Another part is aggregated and grown into a large γ' phase (Fig. 12, refer to plate no. 9). This type of processes apparently enhances persistent strength and persistent plasticity (Fig. 5); hardness is also enhanced. In the T12 process, enhancement of properties is the most apparent.

Further test proof for T0, T7 and T12 processes: the slow-cooling with remelting heat-treatment process and isothermal heat-treatment process can not only enhance persistent properties at 940°C, but also can enhance the 750 and 850°C persistent properties by several fold, in eliminating the crack-tip sensitivity of 750°C persistent strength of the alloy; the impact toughness and high-temperature elongation properties (Table 2) can also be enhanced.

As proved by the aforementioned results, coordination between the strength of the grain boundaries and intracrystal strength is very important. After air-cooling treatment, although the intracrystal strength (hardness) is higher, the grain boundaries are still level and straight; therefore, the persistent service life (esepcially the plasticity) is low (Fig. 2 and Table 2). After slow-cooling treatment, although the grain boundaries are wavy, persistent strength is enhanced while the intracrystal strength is lower, cancelling out the beneficial function of the wavy grain boundaries. Hence, only plasticity is enhanced but not strength (Fig. 3). The isothermal process is the compromise between the air-cooling and slow-cooling processes corresponding to a faster slow-cooling process, to obtain relatively wavy grain boundaries and relatively high intracrystal structure, thus enhancing both the persistent service life and plasticity (Fig. 4). The slow-cooling with remelting process is the integration of air-cooling and slow-cooling processes, sufficiently utilizing the intracrystal strength obtained after air cooling and wavy grain boundaries with slow cooling. Therefore, the enhancement of persistent strength is more pronounced (Fig. 5 and Table 2).

Table 2. Persistent properties, high temperature elongation properties, and room-temperature impact value of three processes (T0, T7 and T12).

热处理方案(1)	(2) 持久性能* 温度, °C(5)	应力 kg/mm² (6)	持续时间 小时：分(7)	δ_5, %	ψ, %	(3) 拉伸性能* 温度, °C(5)	σ_b kg/mm²	δ_5, %	ψ, %	室温 a_k值(4) kg·m/cm²
T0	750 (缺口)(8)	59	75：25							
	750 (光滑)(9)	59	154：20	2.4	2.2	—	—	—	—	0.86
	850 (光滑)(9)	35	196：40	4.1	4.2	850	85.2	5.0	5.2	
	940 (光滑)(9)	22	67：50	5.5	6.8	950	57.8	11.8	14.0	
T7	750 (缺口)(8)	59	>797：30							
	750 (光滑)(9)	59	434：00	10.3	13.2	750	99.5	9.9	17.3	
	850 (光滑)(9)	35	278：30	9.6	13.2	850	87.0	13.4	19.6	—
	940 (光滑)(9)	22	73：50	8.5	9.3	950	57.1	15.8	26.7	
T12	750 (缺口)(8)	59	>785：50							
	750 (光滑)(9)	59	623：00	7.9	8.0	750	100.9	7.2	10.6	
	850 (光滑)(9)	35	342：00	—	15.8	850	88.0	8.7	11.3	1.72
	940 (光滑)(9)	22	80：50	7.8	11.6	950	59.2	16.5	22.4	

* The mean value of three test specimens.
Key: (1) Processes of heat treatment; (2) Persistent properties*; (3) Elongation properties*; (4) Room temperature, a_k value; (5) Temperature; (6) Stress; (7) Persisting time--hours: minutes; (8) Crack tip; (9) Smooth.

3.2. Causes of enhancing persistent properties by wavy grain boundaries

As proved by the test results, strength and plasticity can be significantly enhanced by matching wavy grain boundaries with appropriate intracrystal structure. The following comments can be made on this case. Many researchers prove [10] that there are two types of known fractures along crystals: (1) a wedge-shaped fracture along crystals with cavities forms at the trifurcate grain boundaries, and (2) a hole-type fracture along crystals with formation of circular cavities; this is not related to trifurcate grain boundaries. Under high stress, trifurcate wedge-shaped fractures form at the trifurcate grain boundaries; and under high temperature low stress, hole type fractures of grain boundaries appear. According to the fracture model with slippage of the grain

boundaries, after slip of grain boundaries at high temperature, stress is concentrated at the discontinuous portion of the grain boundaries, or the trifurcate grain boundaries. When stress concentration exceeds the interatomic binding force along the faces of the grain boundaries, a fracture originates. According to the formula presented by McLean [11]:

$$\sigma_s \geq \sqrt{12rG/\pi L}$$

In the equation, σ_s is the shearing stress required for a steady wedge-shaped crack at trifurcate grain boundaries; r is the new surface energy at the unit fracture surface; G is the shearing modulus; and L is the slip length at the grain boundaries. The shearing stress σ_s required to form a wedge-shaped crack at trifurcate grain boundaries is inversely proportional to the square root of slip length L of the grain boundaries. When the grain boundaries are level and straight, L is the length of a side of a crystal grain. When the grain boundary is of sawtooth (wavy) shape, L is the length of a side of the sawtooth. Therefore, following the bending of the grain boundaries, L decreases and hence σ_s increases, thus obviously hindering the appearance of a wedge-shaped crack. At low-temperature high stress, mainly wedge-shaped cracks appear along the crystal fracture. With increasing temperature, stress is reduced, gradually becoming mainly a hole-type fracture. Hence, wavy grain boundaries are the most effective to increase medium-temperature persistent strength (mainly wedge-shaped fracture); for example, most apparent in enhancement of 750°C persistent strength (in the T12 process, the persistent service life is raised about three times, refer to Table 2). Next is the 850°C strength (in the T12 process, the persistent service life is raised about 75 percent); and further down in enhancement is 950°C strength (in the T12 process, the persistent service life is raised about 20 percent).

As proved by facts [10], the slip terrace forms at grain boundaries by crystal deformation; the predominating spots where cavities form are intersections of crystal and sub-crystal boundaries. At intersecting spots of the faces of the grain boundaries and the slip belt, there are small holes at intervals of the grain boundaries. Hence, the wavy grain boundaries should be matched with the appropriate intracrystal strength. If the resistance against transformation of the crystal grains is too low (such as T1-T4 processes), more

slip terraces will form at the faces of the grain boundaries, forming more cavities and holes which do not enhance persistent strength.

3.3. Change of intracrystal structure during slow cooling and during the formation process of wavy grain boundaries

There are quite a few studies on the formation regime of wavy grain boundaries. The wavy grain boundaries of this alloy (GH220 alloy) are formed during the slow-cooling process after solid-solution treatment. In the slow-cooling process when passing through the $\gamma+\gamma'$ two-phase zone, first the γ' phase forms inhomogeneously-shaped nuclei and then grows, inducing migration of grain boundaries and forming wavy grain boundaries [4]. The paper [12] derives a model of the formation process of the grain boundaries. The slower the cooling rate, the larger is the γ' phase of the grain boundaries; the more apparent the migration of grain boundaries, the greater is the degree of bending of grain boundaries. With increasing cooling rate, the precipitation of the γ' phase of grain boundaries gradually and homogeneously have smaller number of mass points; thus, it is difficult to cause migration of the grain boundaries. Therefore, the bending degree of the grain boundaries is smaller following isothermal treatment; the grain boundaries are level and straight following air-cooling treatment.

The cooling rate after solid-solution treatment has a major influence, similarly, on intracrystal structure. The precipitation process of the γ' phase from the over-saturated solid-solution is similar to the tree-branch-shaped crystallization process [13] during condensation of metal from the liquid form. During slow cooling, the intracrystal γ' phase is also inhomogeneously precipitated, in petal-shaped distribution. This structure does not enhance strength. The smaller the cooling rate, the more inhomogeneous is the precipitation. When the cooling rate is increased (in the case of air cooling), the degree of supercooling is increased; the γ' phase tends to homogeneously precipitate to enhance the intracrystal strength.

Therefore, when studying the heat-treatment processes of wavy grain boundaries, attention should be paid not only to how to obtian wavy grain boundaries, but also attention should be given to change of intracrystal structure

to coordinate between the appropriate intracrystal structure and wavy grain boundaries. Otherwise, the strengthening effect will not be attained.

IV. Conclusion

1. For the GH220 alloy, air-cooling heat-treatment process can only obtain level, straight grain boundaries with lower strength and plasticity. By using slow-cooling heat-treatment process, wavy grain boundaries can be obtained, thus apparently enhancing the persistent plasticity but with slightly lowered persistent strength. The isothermal treatment process and slow-cooling with remelting heat-treatment process can apparently enhance the persistent strength and plasticity.

2. The wavy grain boundaries can definitely enhance persistent propertirs of the alloy, but the strengthening result can only be exploited with coordination of appropriate intracrystal strength.

3. T12 and T7 processes are apparently superior to the standard heat-treatment T0 process; the authors recommend their adoption.

LITERATURE

(1) Betteridge, W.and Franklin, A.W., J. Inst. Metals, 85(1956/57), 473.

(2) Weaver, C.W., J. Inst. Metals, 88(1959/60), 462.

(3) Miyagawa, O., Yamamoto, M.and Kobayashi, M., Superalloys, Metallurgy and Manufacture, 1976, 245.

(4) Larson, J.M.and Floreen, S., Met. Trans., A 8A(1977) Jan., 51.

(5) Merrick, H.F.and Floreen, S., Met. Trans., A 9A(1978), Jan., 231.

6. GH118 section: Exploration of Heat Treatment Technique of Sawtooth Structure of Grain Boundaries of GH118 Alloy, Fifth Plant, Shanghai Steel Mill, Internal Use Only Information, 1974.

7. Betteridge, W., The Nimonic Alloys, 1974.

8. Feng Weixi et al, Exploration of Heat Treatment Process of Wavy Grain Boundaries of GH37 Alloy, Beijing Aeronautical Materials Research Institute, Internal Use Only Information, 1978.

9. Tian Shifan et al, Effects on Structure and Properties of GH118 Alloy by Slow-cooling Heat-treatment Process, Beijing Aeronautical Research Institute, Internal Use Only Information, 1980.

10. Watanabe and Tadao, Metal Materials Abroad, 1979, No. 4, pp. 58-65.

11. McLean et al, J. Inst. Met., 85 (1956/57), 468.

12. Zhong Zengyong et al, Preliminary Discussion on Formation Causes of Wavy Grain Boundaries in High Temperature Alloy Regarding High Alloyed Transformation, Iron and Steel Research Institute, 1981.

13. Seregin, G. V., Fizikha Metallov i Metallovedenie [Physics of Metals and Physical Metallurgy], Issue No. 3, 1980. pp. 547-552.

EFFECT OF HEAT TREATMENT ON FINE STRUCTURE AND MECHANICAL PROPERTIES IN ULTRAHIGH STRENGTH STEELS

Zhong Bingwen and Zhang Lianrong

The fine structure of martensite, the type, morphology, and distribution of carbide precipitate, and the distribution of retained austenite in matrix were investigated by transmission electron microscope. The relation between mechanical properties and martensite substructures was also studied. The results indicated that there are some microtwins in lath martensite. Preferential precipitation of cementite was frequently observed at boundaries of these microtwins. The decomposition of retained austenite during tempering occured in company with a diffusion process of carbon. One of the decomposition products is stringer-like cementite. The crystallographic orientation between interlath cementite and tempered martensite does not comform to the well-established Bagaryatskii orientation relationship. The decomposition of retained austensite during tempering belongs to upper bainitic reaction. The starting temperature of the decreasing of impact toughness is coincident with that of the decomposition of interlath retained austenite into stringer of cementite at these boundaries. The retained austenite in net form retarded the crack propagation rate.

FOREWORD

The 30CrMnSiNi2A and 40CrMnSiMoVA steels are low alloy high strength structural steels. These steels are used mostly to make major structural members of an aircraft in the aviation industry. In some aircraft models, main

beams and landing gears made of these steels often had early-stage fatigue fracture, leading to early-stage fracture. Therefore, extensive study of these steels, of their heat treatment technique, micro-structure, fine structure and relations among these properties, constitutes an important problem in order to improve the heat-treatment technique and prolong service life of the structural members. This paper describes the use of thin films to test directly specimens with transmission electron microscopes; studies were made of the fine structure of different heat-treatment states of these two steels with isothermal quenching. Comparison tests of properties were also made. The paper discusses the effect on the ductility index and da/dN of the dissolving characteristics and fine structure of the retained austenite, and the orientation relations among martensite, austenite and carbide.

Table 1 shows the chemical composition of raw materials used by the aforementioned steels.

Table 1. Chemical composition of materials

材料代号 (1)	(2) 化学成分，重量%						
	C	Si	Mn	Cr	Ni	Mo	V
A	0.40	1.60	1.20	1.50	—	0.5	0.10
B	0.30	1.00	1.00	1.00	1.60	—	—

Key: (1) Code of materials; (2) Chemical composition, weight percent.

TEST RESULTS AND DISCUSSIONS

1. Structure

(1) Matrix structure: Observations through a transmission electron microscope were made on specimens of the two aforementioned steels following different isothermal treatments. Table 2 lists the overall structural characteristics. Within the range of test temperatures, all matrix structure is $M_{tempering}$+$B_{lower\ bainite}$ with isothermal treatment at temperatures less than

or equal to 300°C. The fasciculation trend of martensite for steel A is lower than that of steel B.

(2) Sub-structure of martensite: within the range of test temperatures shown in Table 2, the sub-structures of martensite of two types of steels are close. In laths of bundle-distributed martensite, there are also distributed the twin relations in addition to distribution with large and small angles. The property of twin-relationship distribution is that no retained austenite exists within the dislocation martensite (Fig. 1, refer to plate No. 10 [not available in xerox copies of text]). The twin boundaries are frequently the positions of predominant precipitation of brittle carbide. The formation of this type of twins is related to the homogeneity of the material composition. If the temperature for becoming austenite is not high enough and the time of temperature preservation is short, local aggregation will occur for some alloy elements, such as Cr, Mn and Ni, thus changing the phase-change properties in some zones. Therefore, in the process of phase transformation of austenite, twins form in local zones of dislocation martensite. Of course, local twin martensite may also form.

For tempering at temperatures less than or equal to 400°C, the precipitation of carbide within laths is not much. With tempering at temperatures less than or equal to 300°C, there are small quantities of precipitation of ε-carbide for two types of steel. With tempering of steel B at temperatures below 350°C, the ε-carbide has not been completely dissolved. Under the temperature where A_r apparently begins to dissolve, frequently carbide within laths aggregates and grows.

(3) Distribution and dissolution of retained austenite: Some researchers include all retained austenites in the (M-A) structure [11]; the distribution properties are related to volume percentage and heat treatment technique. Those austenites distributed in laths are mostly block-shaped; those distributed in interlath spaces are mostly thin-film-shaped or stringer-like (Figs. 2 and 3, refer to plate No. 10 [not available in xerox copies of text]). In the situation of the same isothermal temperature and time, the volume percentage of A_r in steel A is higher than that in steel B, but its distribution is not as homogeneous as in steel B.

Table 2. Heat treatment technique and structural properties.

(1) 材料代号	试样编号 (2)	热处理工艺 (3)	(4) 组织组成物*	(5) 精细结构特征
A	A_1	900°C加热, (6) 180°C等温+(7) 260°C回火 (8)	M回+B下+A_r+C (9)	M回或B下边界与点在薄膜状或条状A_r，有的板条内也存在A_r。有的板条马氏体内存在局部孪晶。渗碳体沿此边界优先析出 (11)
	A_2	900°C加热, (6) 250°C等温+(7) 260°C回火 (8)		发现自α/A_r相界A_r处析出ε-碳化物，其余同上 (12)
	A_3	900°C加热, (6) 300°C等温 (7)		边界A_r较多，呈薄膜状或条状，其余同A_1 (13)
	A_4	900°C加热, (6) 300°C等温+(7) 300°C回火 (8)		同A_3，从300°C下回火。已观察到奥氏体发生分解 (14)
	A_5	900°C加热, (6) 300°C等温+(7) 400回火 (8)	M回+B下+A_r+C (9) 但A_r很少 (10)	M回或B下边界变得模糊。A_r大量分解，在板条边界上形成串状渗碳体，未观察到局部孪晶 (15)
B	B_1	920°C加热, (6) 230°C等温+(7) 300°C回火 (8)	M回+B下+A_r+C (9)	和A钢的A_1相近 (16)
	B_2	920°C加热, (6) 230°C等温+(7) 350°C回火 (8)		边界A_r已不连续，且开始明显分解，ε-碳化物尚未完全溶解 (17)
	B_3	920°C加热, (6) 230°C等温+(7) 400°C回火 (8)		A_r大量分解，在边界存在串状碳化物 (18)
	B_4	920°C加热, (6) 300°C等温+(7) 400°C回火 (8)	M回+B下+A_r+C (9) 但A_r甚少 (10)	A_r的分解规律和230°C等温的相近，在边界形成更大的脆性渗碳体 (19)

* $M_{tempering}$--tempered martensite; $B_{lower\ bainite}$--lower bainite; A_r--retained austenite; C--cementite.

Key: (1) Material code; (2) Number of test specimens; (3) Heat treatment technique; (4) Structural composition*; (5) Properties of fine structure; (6) Heating; (7) Isothermal treatment; (8) Tempering; (9) $M_{tempering}$+$B_{lower\ bainite}$+A_r+C; (10) But very little A_r; (11) Existence of thin-film-shaped or stringer-like A_r at boundaries of $M_{tempering}$ or $B_{lower\ bainite}$; A_r also exists in some laths. Local twins exist in some other lath martensite. Cementite is predominantly precipitated along this boundary; (12) It is discovered that ε-carbide is precipitated at the phase boundary A_r of α/A_r; the others are the same as above; (13) more A_r (thin-film-shaped or stringer-like) at boundaries; the others are the same as A_1; (14) Same as A_3, tempering at temperatures below 300°C. It has been observed that austenite is dissolved; (15) Boundaries of $M_{tempering}$ or $B_{lower\ bainite}$ blurred. Large quantities of A_r dissolved, forming stringer-like cementite at lath boundaries but without observation

[Key continued on following page]

[Key continued from preceding page]

of local twins; (16) close to A_r in steel A; (17) Boundaries of A_r become discontinuous with beginning of apparent dissolution; ε-carbide not completely dissolved yet; (18) Large quantities of A_r dissolved and existence of stringer-like carbide at boundaries; (19) The dissolution rule of A_r is close to that of isothermal treatment at 230°C; formation of larger brittle cementite at boundaries.

Comparing the data in Figs. 2, 3 and 4 (refer to plate No. 10) and Table 3, we can see the dissolution situation of A_r with tempering temperature after the isothermal quenching process of these two steels. With tempering at temperatures below 400°C, the interlath stringer-like carbide of martensite (or bainite) in steel A is larger than that in steel B; however, the dissolving rate of the stringer-like carbide of steel A is lower than that of steel B. It follows that the lower limit of brittleness-forming temperature of steel A is higher than that of steel B. This is because steel A has more silicon, enhancing the resistance to tempering; thus, the brittleness-forming zone of the tempered martensite is pushed to a higher temperature.

With four hours of cooling treatment at -60°C following isothermal treatment, the volume percentage of A_r does not change much (Fig. 5). This reveals on the one hand the existence of silicon in the steel by changing the thermodynamic conditions of carbide precipitationin steel, enhancing the thermal stability of A_r. On the other hand, it reveals that in the quenching structure of this type of steel, A_r is mainly retained by mechanical factors. These are the properties of silicon-containing steel.

2. Orientation relationship between matrix and carbide and dissolving properties of A_r

Based on diffraction analysis and matrix calculation [2], the marking results of various diffraction spectra are derived as follows:

$$[011]_\gamma // [233]_\gamma // [0\bar{2}1]_\varepsilon \quad \cdots\cdots (1)$$
$$(2\bar{1}1)_\gamma // (3\bar{1}\bar{1})_\gamma // [112]_\varepsilon$$

$$[\bar{1}00]_\gamma // [0\bar{1}1]_\gamma // [\bar{1}22]_\varepsilon \quad \cdots\cdots (2)$$
$$(002)_\gamma // (200)_\gamma // (0\bar{1}\bar{1})_\varepsilon$$

$$[\bar{1}11]_\gamma // [0\bar{1}\bar{1}]_\gamma // [0\bar{1}0]_\varepsilon \quad \cdots\cdots (3)$$

$$(101)_\gamma // (\bar{1}\bar{1}1)_\gamma // (103)_\varepsilon$$
$$[012]_{\gamma 1} // [013]_{\gamma 2} // [012]_{\varepsilon 1} // [\bar{2}01]_{\varepsilon 2}$$
$$(200)_{\gamma 1} // (200)_{\gamma 2} // (021)_{\varepsilon 1} // (1\bar{1}2)_{\varepsilon 2}$$
$$\cdots\cdots (4)$$

Table 3. Variation of dot matrix constant of austenite while dissolving.

材料代号 (a)	热处理工艺 (b)	A_r, %	A_r 分解率, % (c)	a_0, 点阵常量 (d) $(200)A_r$
A	300°C等温 (e)	13	0	未测 (g)
	300°C等温(e)+300°C回火(f)	11.8	9.2	3.618
	300°C等温(e)+350°C回火(f)	10.0	23	3.612
	300°C等温(e)+400°C回火(f)	7.1	45	3.602
B	300°C等温(e)	9	0	未测(g)
	300°C等温(e)+300°C回火(f)	7.1	21	3.610
	300°C等温(e)+350回火(f)	6.0	33	3.605
	300°C等温(e)+400°C回火(f)	5.0	66	3.600

Key: (a) Code of material; (b) Heat treatment technique; (c) Dissolving rate; (d) Dot matrix constant; (e) Isothermal treatment; (f) Tempering; (g) Not measured.

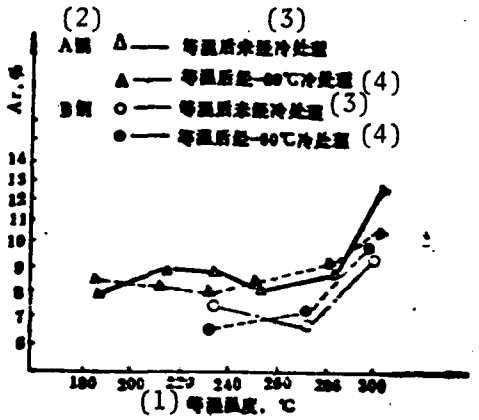

Fig. 5. Relationship between volume percentage and isothermal temperature of retained austenite in test specimens of steels A and B.
Key: (1) Isothermal temperature; (2) Steel; (3) Without cooling treatment after isothermal treatment; (4) With cooling treatment at -60°C following isothermal treatment.

Equation (1) shows the marking result of the diffraction spectrum in Fig. 6 (refer to plate No. 11 [not available in xerox copies of text] for test specimen A_1. The orientation on intervals of γ/Fe_3C satisfies the "B relations"

[3]; and orientation on intervals of γ/α satisfies the "K-S relations" [4]. Although there are certain orientation properties on intervals of γ/Fe_3C, but because the orientation on intervals of α/Fe_3C satisfies the "B relations", it follows that Fe_3C in lower bainite is precipitated from ferrite.

Equation (2) shows the marking result of the diffraction spectrum of Fig. 7 (refer to plate No. 11 for A_2 test specimen [not available in xerox copies of text]). The orientation on intervals of α/ε-carbide satisfied the "Jack" relations [5]; and on intervals of α/γ satisfies the "K-S relations". We can see from Fig. 7 that the wave-like ε-carbide in the dark field image also maintains certain orientation properties on intervals of ε/γ.

As revealed in tests, the tempering temperature of A_1 test specimens is lower; no dissolution occurs in A_r. We also can see from Fig. 7 that austenites at boundaries of the ε-carbide and α/γ phase are connected to each other. By combining with Eq. (2), it can be considered that the ε-carbide in lower bainite is precipitated from the austenitic side of α/γ phase boundaries. However, due to growth of ferrite in the isothermal process, the carbide is enveloped by ferrite; therefore, the carbide is shown in the dark-field image as lying over the ferrite phase.

Equation (3) shows the marking result of the diffraction spectrum of the A_4 test specimen in Fig. 3. There is the relationship $\begin{matrix}(\bar{1}11)_\alpha \,//\, (0\bar{1}0)_\varepsilon \\ (101)_\alpha \,//\, (103)_\varepsilon\end{matrix}$ on intervals of α/Fe_3C; the relationship is close to the "B relations" but not the "B relations" themselves. The relationship matches the "U relations" [6]. The "U relations" are the result of comprehensive development of "Pitsch relations" on intervals of α/Fe_3C [7] and "K-S relations" on intervals of α/γ; therefore, in this situation, the orientation on intervals of α/Fe_3C actually satisfies the "Pitsch relations". With direct observation and measurement of A_r, the tempered A_r at 300°C has been dissolved. From this, we can prove that Fe_3C is precipitated by directly dissolving A_r at boundaries of the α/γ phase.

Equation (4) is obtained from the B_4 test specimen (Fig. 4 [not available in xerox copies of text]). As proved based on a diffraction analysis method

similar to those mentioned above, the orientation between the tempered martensite and the interlath cementite does not satisfy the "B relations"; this reveals that the interlath carbide is not precipitated from the tempered martensite. We can see from Fig. 4 that at places with distribution of the original interlath A_r, there are stringer-like cementites. This also proves the direct dissolution characteristic of interlath A_r. Some researchers [8] consider that this type of dissolution regime is an upper bainitic reaction.

As revealed by data in Table 3, with dissolution of A_r, its dot matrix constant (a_o) gradually lowers; this is a direct manifestation of gradually decreasing carbon atoms in austenite.

From the aforementioned, with direct observation through an electron microscope, from the variation trend of a_o at the dissolution of A_r, and from analysis of the orientation relations, it can be thoroughly proved that in the tempering process of A_r, the direct product of thermal dissolution are brittle cementite and carbon-deficit austenite, which is mechanically unstable, and it can easily change into not-yet-tempered martensite under the action of stress. In the original structure with an abundance of A_r, the stringer-like cementite (produced in the interlath spaces following dissolution of A_r) is larger. It follows that in the isothermal structure of steel, the volume percentage, distribution properties and the dissolution change of A_r can have apparent effects on properties like ductility and plasticity.

3. Structure and properties

(1) Dissolution and ductility of retained austenite: Figure 8 shows the effect on properties of isothermal structure of steel A by the tempering process at different temperatures. We can see from Fig. 8 that the a_k value of steel A begins to decrease with tempering in the vicinity of 300°C; this is related to beginning dissolution of A_r at 300°C tempering. In addition, for test specimens of isothermal (300°C) treatment, the trend of decreasing a_k value is greater than in (180°C) isothermal treatment. The cause is that more A_r exists in the former [isothermal treatment at 300°C] than the latter

[isothermal treatment at 180°C], forming more brittle carbide during dissolution and a greater effect on a_k.

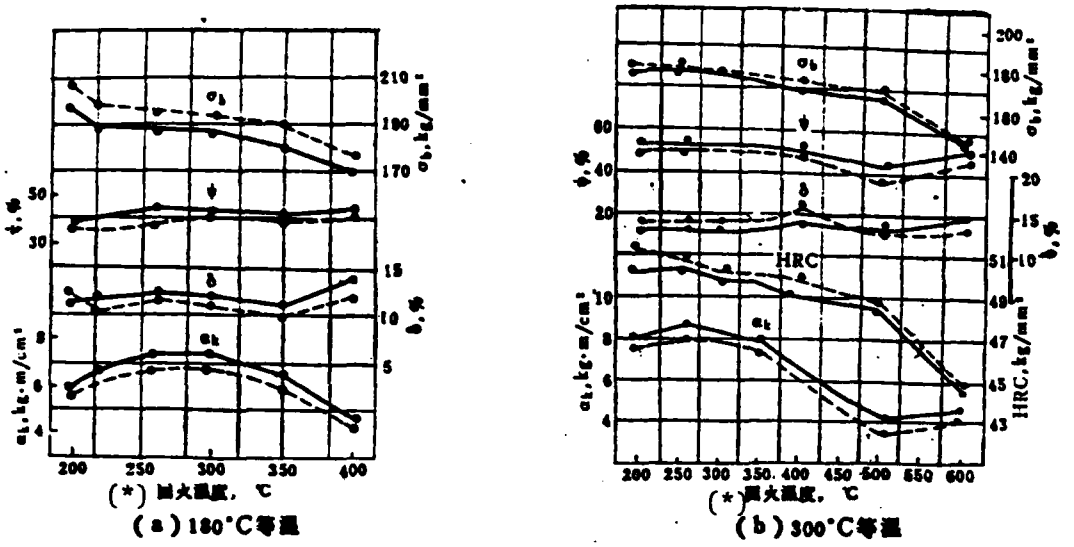

Fig. 8. Properties of tempering at different temperatures following isothermal treatment of steel A: (a) Isothermal treatment at 180°C, ____ carbon content at 0.42; (b) Isothermal treatment at 300°C, ____ carbon content at 0.37.
Key: (*) Tempering temperature.

The dissolution rule of A_r in steel B is close to that of steel A. If we compare the characteristic curve in Reference [1], we still can see that the a_k value in the vicinity of 300°C begins to decrease; this is also consistent with the tempering temperature of A_r dissolution.

In these two tests with tempering of the test steel specimens at temperatures below and equal to 300°C, besides the elimination of internal stress caused by isothermal quenching, there is little precipitation of ε-carbide, and only small quantities of increase of ψ and δ. In short, for tempering at temperatures below or equal to 400°C, the other properties have changed but little besides the a_k value. It follows that, although indexes of ductility and plasticity of steel are the comprehensive reaction of properties of volume percentage, distribution characteristics, impurity aggregation, local twins, and martensite of A_r, still as viewed from the point of view of consistency

between the tempering temperature of A_r dissolution, and the temperature of beginning decrease of a_k value, the dissolution characteristics of A_r and its volume percentage are an important factor influencing indexes of ductility and plasticity.

(2) Ductility phase and da/dN: Figure 9 shows the da/dN--ΔK curves of tempering test specimens for temperatures close to one another following isothermal treatment of these steels at different temperatures. Since there are differences in strength levels of these two steels and in the properties of fine structure of composition phases, it is difficult to accurately compare the da/dN properties of the two types of steels. However, we can qualitatively say that the carbon content in steel B is lower, containing 1.6 percent Ni; in addition, the interlath distribution of A_r is relatively homogeneous, mostly film-shaped. Therefore, during extension of cracks, the probability of A_r occurring is higher; this causes greater absorption of extension energy of the crack. Therefore, under the condition of identical K values, the extension rate of a crack in steel B is lower.

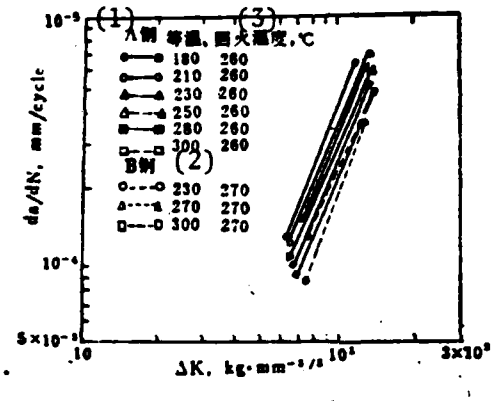

Fig. 9. da/dN--ΔK curves of A and B steels.
Key: (1) Steel A; (2) Steel B; (3) Isothermal and tempering temperatures, °C.

For the same type of steel, the effect on matrix structure of low-temperature tempering is little. Only with increase of isothermal temperature are the volume percentages of $B_{\text{lower bainite}}$ and A_r increased somewhat. The effect on crack extension of A_r is considerably greater than that of bainite. Based on

an estimated calculation of plasticity work by relative contents of A_r and martensite in 4340 steel, the contribution of 10 percent A_r is three times higher than of 90 percent martensite. It is apparent that with increase of isothermal temperature ($\leq$300°C), under the same value of ΔK, the gradual decrease of da/dN has an important function on A_r. Though the resistance against crack extension is related to micro-structure and fine structure properties within the plasticity zone of the crack tip, it can be expected that for A_r within the plasticity zone, the intensification of the strain phase change under the action of periodic stress can cancel out the softening function of martensite and bainite. A_r also has some slowing function on the crack extension.

In short, with a certain volume percentage and uniform distribution, the interlath A_r of stability of homogeneous distribution is effective to increase crack extension resistance and decrease da/dN: (1) A_r can branch out the crack, so the crack extension is discontinuous; and (2) A_r within the plasticity zone can, on one hand, produces plasticity flow variation for crack dulling, and on the other hand, cancels out some stress concentration due to elimination of partial stress concentration by strain phase-change plasticity. As proved by studies in paper [10], under the action of stress at certain periods, in the martensite time-effect steel, the interlath stable A_r can effectively lower the da/dN value in the low-speed extension zone of the crack in the vicinity of the threshold value. Generally speaking, A_r is still a metastable phase; its effect on properties is determined by environmental and loading conditions [11].

CONCLUSIONS

1. In two tests of steel, there are small quantities of local twins in lath martensite. Boundaries of the twins are often the locations of predominantly precipitated brittle carbide.

2. During dissolution of retained austenite, the dissolution properties of directly precipitated carbide show an upper bainitic reaction.

3. The tempering temperature during the start of relatively apparent dissolution of retained austenite is consistent with the tempering temperature of a decreasing a_k value. For a greater quantity of original retained austenite, the degree of brittleness is more pronounced. The retained austenite has an apparent slowing-down function on crack extension.

The authors thank colleagues Liu Caimu, Ouyang Hui and Wang Guangsheng, among others, for their support and assistance on the paper.

LITERATURE

1. Kang Mokuang et al, (M-A) Structure in Low Alloy High Strength Structural Steel, Scientific and Technical Materials, Northwest Industrial University, 1979.

2. Li Chunzhi, WULI XUEBAO [JOURNAL OF PHYSICS], 28 (1979), 314.

3. Bogaryatskiy, Yu. Doklady ANSSSR [Papers of USSR Academy of Sciences], 73 (1950), 1161.

[4] Kurdjumov-Sachs, G., Z.Phyzik., 64 (1930), 325.
[5] Jack, K.H., (JISI), 196 (1951), 26.
[6] Chmori, Y., Trans. ISIJ, 13 (1973), 56.
[7] Pitsch, W., Acta Met., 101 (1962), 897.
[8] Narasimha Rao, B.V., Thomas, G., Met. Trans., 11A (1980), No.3,441.
[9] Karl-heinz Schwable, Engng. Fracture Mech., 9 (1977), No.4. 795.
[10] Richie, R.O., J. Engng. Mater. Technol., Trans. ASME Series, 99 (1977), 195.
[11] Paker, E.R., Met. Trans., 3A (1978), No.3, 439.

STUDY OF THE FRACTURE TOUGHNESS OF AIRCRAFT ACRYLIC SHEETS

Chen Ruoxi, Shao Yujun and Fan Tang

Considerable works on the fracture toughness of glassy polymers have been done, yet there were still controversies about the definition of K_{Ic}. In this paper, the author attempted to discuss the plane strain fracture toughness K_{Ic} of PMMA(polymethyl methacrylate) based on the theory of linear elastic fracture mechanics and the intrinsic characteristics of macromolecular motion in polymeric materials. The effects of the absorbed water in material, environmental humidity and humid air aging at elevated temperature on the fracture behaviours of two kinds of acrylic sheets, YB-3 and YB-4, were studied. It was found that the present of water or humidity is of benefit to the fracture resistance of PMMA materials.

I. Foreword

With gradually maturing application of linear elastic fracture mechanics in metal materials, starting from the 1960s there were researchers abroad who applied the linear elasticity fracture theory to brittle vitreous polymer materials. However, there is a particular molecular movement in polymer, since its crack face is entirely different from that of metals, with a very wide range of slow extension zones of fissures. Therefore, there are many different opinions [1-5] on how to determine the fracture toughness K_{1c} of organic glass PMMA. The determination value of K_{1c} of PMMA is different in different studies, with a wide range of differences (700 to 1750 psi $\sqrt{\text{in}}$). Thus, there are difficulties

in designing the damage limit. Following long-term storage of YB-4 aviation PMMA, its elongation strength drops, apparently because it absorbs moisture. Therefore, for a long time researchers have been concerned about the effect of water on glass (with fissures) in terms of its mechanical properties.

The paper emphasizes the correct definition of fracture toughness of organic glass.

II. Experimentation

The test materials are YB-3 and YB-4 aviation PMMA; specimens of a center crack test were used; refer to Fig. 1 showing dimensions of the test specimen, 200x50x10 mm. In order to ensure processing quality of the center crack, a special die was used to process the fissure. Then, a fatigue fissure was cut in advance on a test machine. Three methods were used to pre-treat all test specimens: (1) according to ASTM D_{618} specifications, the test specimens were placed in a standard laboratory environment (23±1°C and relative humidity at 50±2 percent) for four days of treatment; (2) soaked in 20°C water for 24 horus; and (3) aged for 30 days at 60±1°C and 100 percent relative humidity environment.

Tests proceeded with an Instron 1253 test device with indoor temperature at 18 to 22°C and relative humidity at 55 to 70 percent; refer to instruments and method recommended by the ASTM standard method of fracture toughness tests of plane strain of metal materials [6]. An X-Y recording device was used to record the load-crack-displacement curve. The moving speed of the fixture was maintained at 0.5 mm/min; a tool microscope was used to measure the crack length at the measurement cross section. The length of the crack at its initiation and the crack length during transition from slow to fast extension of cracks were calculated separately.

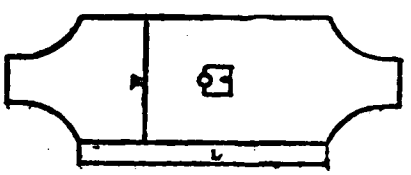

Fig. 1. Test specimen of crack toughness of PMMA.

According to formulas recommended by reference [7], the factor of stress intensity is calculated:

$$K=\frac{P}{BW}\sqrt{\frac{\pi a}{2}}\left[1-0.025\left(\frac{a}{W}\right)^{2}+0.06\left(\frac{a}{W}\right)^{4}\right]\sqrt{\sec\frac{\pi a}{2W}} \qquad (1)$$

In Eq. (1), the error of any ratio value of a/W is less than 0.1 percent.

The meaning of various symbols represented is as follows: K is the factor of stress intensity in $kg/cm^{3}/^{2}$; B is the thickness of the test specimen in cm; W is the width of the test specimen in cm; and P is the critical load in kg. As specified in reference [6, 8], the value of P_5 is taken for P; this is the load corresponding to the intersecting point of the curve and the chord with inclination lowered by 5 percent in the load-displacement curve passing through the origin. a is the overall length (in cm) of the center crack. Calculated using the three following equations, the effective crack lengths $\bar{a}$, $\bar{a}_3$ and $\bar{a}_5$ with equivalent effect of the front fringe of the actual crack can be derived (refer to Fig. 2):

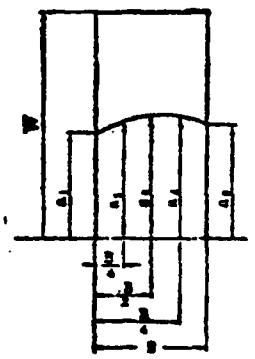

Fig. 2. Schematic diagram for crack measurement.

$$\bar{a}=\frac{1}{3}(a_2+a_3+a_4) \qquad (2)$$

$$\bar{a}_3=\frac{2}{3}a_3+\frac{1}{6}(a_1+a_5) \qquad (3)$$

$$\bar{a}_5=\frac{7}{90}(a_1+a_5)+\frac{16}{45}(a_2+a_4)+\frac{2}{15}a_3 \qquad (4)$$

Equation (2) is the calculation formula recommended by reference [6]. The equation is only adapted to the situation of relatively small curvature at the front fringe of the crack. Equations (3) and (4) were derived by the authors based on the principle of equal effectiveness of softness, separately suitable to the application of measuring three or five points.

III. Test Results and Discussion

3.1. Fracture criterion of brittle high polymer materials

Owing to particular characteristics of molecular movement of high polymer materials, the cross-section appearances of the organic glass (PMMA) and polystyrene (PS) are different from that of metal materials, with a sector of relatively wider slow extension (of the crack) zone (Fig. 3). Concerning the correct definition of fracture toughness K_{1c} of organic glass, there is still divergence in opinions. Marshall et al (1973 and 1974) called the factor (K at initiation) of stress intensity at the beginning of the crack extension, and K_{1c} [3, 4], the definition of the factor of stress intensity during transition (of crack extension) from slow to fast speed. Margolis (in 1976) considered that basically the slow steady extension [of crack] in organic glass is brittle extension. The length of the crack at its initiation and the crack length during transition from slow to fast extension of the crack does not relate to the maximum load P_{max} of the load-displacement curve. The most rational method of fracture toughness (in the definition) should consider the two unrelated "instabilities" as the basis: the unsteady load as the basis, K_c (P_{max}, a_c); the unsteady transition from slow to fast speed [of cracking] as the basis, K (extrapolation); and a_c is the crack length [5] corresponding to maximum load P_{max}.

If we start from the fundamental viewpoint of linear elasticity fracture mechanics, the analysis proceeds by combining the characteristics of molecular movement of the high polymers, obviously these two viewpoints have shortcomings.

It is assumed that an object has a two-dimensional crack; the loading condition is shown as in Fig. 4, then the following thermodynamic equilibrium formula applies:

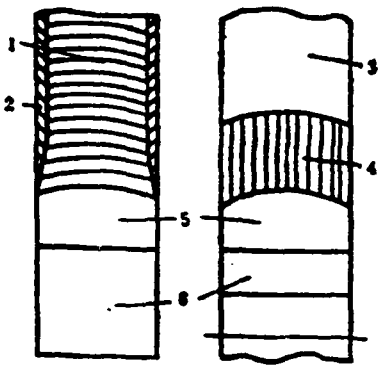

Fig. 3. Comparison of cross-section appearance of test specimen of fracture toughness of steel and organic glass (PMMA): 1--level crack; 2--45° sheared edge; 3--fast fracture zone; 4--slow [crack] extension zone; 5--pre-made fatigue crack; 6--machined notch.
Key: (a) Steel; (b) Organic glass.

$$\frac{dW}{dA}=\frac{dU}{dA}+\frac{dK}{dA}+\frac{dU'}{dA}+\frac{d\Gamma}{dA} \qquad (5)$$

In the equation, W is the work done by the external load; A is the crack area; K is kinetic energy; U is the reversible strain energy stored; U' is the plasticity strain energy; and Γ is the surface energy. In the situation when kinetic energy K=0 or dK/dA =0, the energy dissipation rate is

$$-\frac{d\Pi}{dA}=\frac{dW}{dA}-\frac{dU}{dA}=d\frac{U'}{dA}+\frac{d\Gamma}{dA} \qquad (6)$$

Since the plasticity strain energy U'=2PA and the surface energy $\Gamma=2\gamma A$,

$$d\Pi/dA=2(P+\gamma) \qquad (7)$$

Π is the total potential energy; P is the plasticity strain energy of a unit area; and γ is the surface energy of a unit area.

It is assumed that the material is isotropic, then the following equation can be derived:

$$-\frac{d\Pi}{dA}=\frac{1-\nu^2}{E}K_1^2 \quad \text{(plain strain)} \qquad (8)$$

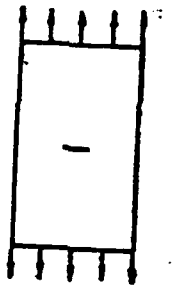

Fig. 4

E and ν are, respectively, the modulus of elasticity and Poisson's ratio of the material. From Eqs. (7) and (8), the revised Griffith fracture criterion [9] can be obtained:

$$K_{Ic}=\sqrt{\frac{2E(\gamma+P)}{1-\nu^2}} \qquad (9)$$

During transition from slow to fast speed of the crack extension, the kinetic energy K (of a vitreous polymer containing cracks) and dK/dA apparently are not equal to zero. Thus, Eq. (7) is not established. Besides, when a crack slowly and persistently extends, both the external boundary and the external load change appreciably; thus, the change of external work (δW) cannot be neglected, and the energy dissipation rate $-d\Pi/dA$ is not equal to the change of strain energy of unit area $\pm dU/dA$. Therefore, Eq. (8) also is not established [10]. Thus, the use of Eq. (9) as the fracture criterion is without the foundation. Therefore, it is a mistake to define the factor of stress intensity (as K_{1c}) during transition from slow to fast [crack] speed. As with metal materials, we should define the factor of stress intensity (as K_{1c}) during initiation of the crack in a vitreous polymer.

Under the action of static loading, silver grains are formed because of high polymer orientation at the crack tip due to stress concentration. In the macroscopic manifestation, it is the appearance of a yielding zone in the front portion of the crack. By comprehending [9, 11 and 12] in the Reference, it is acknowledged that the microscopic structure of silver fissures at the crack tip

should be shown as in Fig. 5. The coarse filaments elongated at the crack tip are actually composed of large molecules of many orientations; they are twined with a certain twining density. Under the action of external loading, even at room temperature the chain sectors and lateral chains of molecules with these orientations in silver grains can still move continuously (alpha process and beta process) to change the structural image to be adaptable to the external force. In the steady stage, the coarse filaments in the silver grains do not break, and the crack also does not extend. Once the factor of stress intensity at the crack tip exceeds the critical value K_{1c}, coarse filaments begin to break one after the other with the beginning of the forward extension of the crack. In the initial stage of crack extension, its speed is relatively slow; the high polymers at the crack tip have sufficient time for orientation. At that time, the major molecular movement is the alpha process. With increasing speed of crack extension, the number of orientation molecules is gradually decreased; the distance from the crack tip to the tip of the silver grains becomes closer and closer [9]; the molecular movement transits to the mixed alpha and beta process. When the crack transits from the slow to the fast extension zone, the molecular movement is again changed into predominantly the beta process; this is formed by molecular movement exclusively for high polymers. At that time, the factor of stress intensity of the crack tip is only the inherent characteristic of high polymer material; the magnitude of the value [of the stress-intensity value] can indicate the general situation of molecular movement of different polymers.

Now, we define the factor of stress intensity during crack initiation of vitreous polymers (such as PMMA) as K_{1c}, the fracture toughness of plain strain; K (instability) is the stress-intensity factor during transition from slow to fast speed of the crack extension. The calculation proceeds by considering separately the pre-made fatigue crack length and the crack length during transition of the extension speed as the effective crack length.

3.2. Calculation of equal-effective crack length

According to the principle of equal effectiveness, there is the same softness in the test specimen at the front fringe of the crack, and in the test specimen at the front fringe of a level, straight crack. At the same time, it is assumed that there is the same cross sectional area of these two cracks. Then,

by using Newton-Cotes' numerical integration formula, formulas (3) and (4) are derived for calculation of equivalent-effectiveness crack length. Compared to Eq. (2), the calculated (by using Eqs. (3) and (4)) equivalent-effectiveness crack length is closer to the crack length at the front fringe of a level, straight crack. The calculation results in Table 1 indicate that the calculation accuracy of Eq. (4) is relatively high, and the accuracy of Eq. (4) also can meet the requirements; the requirement on the curvature of the front fringe of the crack is not as strict as that of Eq. (2); its use is relatively convenient.

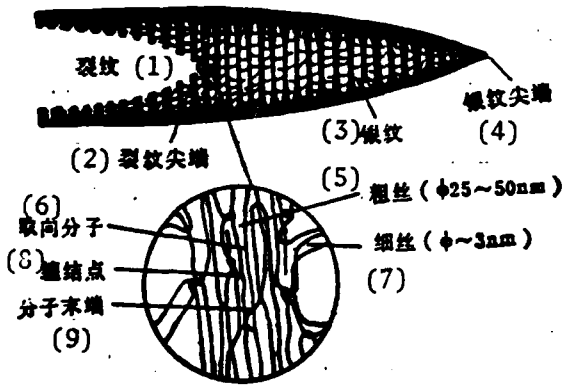

Fig. 5. Schematic diagram of crack of vitreous polymer and microscopic structure view of silver grains.
Key: (1) Crack; (2) Crack tip; (3) Silver grain; (4) Tip of silver grain; (5) Coarse filament; (6) Orientation molecules; (7) Fine filament; (8) Twined point; (9) Terminal of molecule.

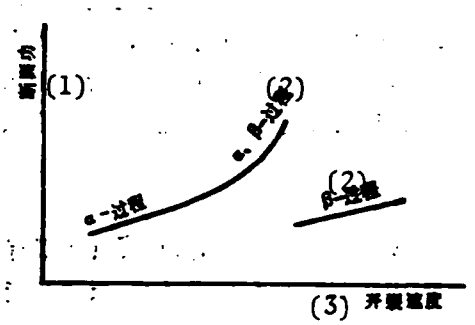

Fig. 6. Relationship between crack [extension] speed and cross-section energy.
Key: (1) Cross-section energy; (2) Process; (3) Speed of crack [extension];

3.3. Effect of water content

Water content has an significant function on crack resistance characteristics of PMMA. Beaument (1975) considered that water plays a major role [13] in the function of the crack tip in increasing the K_{1c} of a vitreous polymer. Williams (1974) discovered that the speed of crack extension is

controlled by water flow in the porous structure of the silver grains [14]. Gilbert (1977) proved that water can plasticize PMMA by the mutual action of local portions of the main chain of large molecules. For the common motion of main and side chains of a polymer, water can play the function of a plasticizer. With increasing water content, the vitrification temperature T_g of PMMA decreases [15].

Table 1. Comparison of fracture toughness of YB-3 glass and YB-4 glass.

试样号 (a)	材料 (b)	试样数 (c)	预处理 (d)	K_{1c}, kg/cm$^{3/2}$			K(失稳), kg/cm$^{3/2}$ (e)		
				1	2	3	1	2	3
301	YB-3	4	(f)标准环境	111.1	110.4	110.6	161.8	161.4	161.3
302	YB-3	4	(g)水浸	111.5	110.5	110.6	163.3	162.1	162.3
303	YB-3	4	(h)湿热老化	104.1	104.0	103.6	153.3	153.3	153.7
401	YB-4	5	(f)标准环境	110.4	110.4	110.3	146.5	146.4	146.4
402	YB-4	3	(g)水浸	110.8	110.0	110.1	142.8	142.3	142.3
403	YB-4	4	(h)湿热老化	108.8	109.1	108.9	129.2	129.3	129.7

Note: Values for "1", "2" and "3" for K_{1c} and K (instability) are derived by calculating the equivalent-effective crack lengths from Eqs. (2), (3) and (4), respectively.

Key: (a) Code of test specimen; (b) Material; (c) Number of test specimens; (d) Pre-treatment; (e) Instability; (f) Standard environment; (g) Soaked in water; (h) Humid heat and ageing.

The water absorbed after 24-hour soaking by YB-3 and YB-4 glass is equivalent to the water absorption quantity (0.10 to 0.16 percent) of specimens put aside at room temperature for three months. However, from data in Table 1, K_{1c} and K (instability) before and after treatment of two types of glass do not change appreciably. The test of completely submerging the crack in water did not proceed due to limitations of test conditions, but Beaument made such tests, discovering that K_{1c} of PMMA increases appreciably, completely eliminating the stage of slow extension of the crack [13]. We can see functions of water flow in the porous structure of the silver grains, and functions of a large

amount of water directly contacting the local portion of the main chain of large molecules as well as the function of side chains; these functions are considerably stronger than water absorption. Besides, the existence of large amount of water can absorb relatively more strain energy; this possibly is the main cause of enhancing fracture toughness.

3.4. Influence of humid heat and ageing

As clearly revealed from data in Table 1, after a 30-day treatment of humid heat and ageing, K_{1c} and K (instability) of both types of glass decrease appreciably. After 27-day treatment of humid heat and ageing under the same conditions for YB-4 glass, its molecular weight did not decrease [16]. Obviously, the lowering of glass properties is not due to change in molecular weight; this is possibly related to a deficiency at the surface of the test specimen due to its long-time exposure in humidity and heat, and can be related to crack branching of the slow-extension stage of the crack, and the uneven phenomenon at the cross section.

3.5. Effect of polarity radical

After treatments with water soaking and in a standard laboratory environment, the fracture toughness K_{1c} of two types of glass is not much different; however, the value of K (instability) of YB-3 glass is considerably greater than that of YB-4 glass (Table 1). This may be related to the difference in mobility of large molecules. At the main chain of large molecules of YB-4 glass, there is a certain amount of high-polarity craboxyl-group (COOH) increasing the intermolecular acting force, thus limiting the mobility of the structural element to reveal greater rigidity of the entire molecule. Conversely, the softness of large molecules of YB-3 glass is better, with low yielding stress. Moreover, it is easier to enable the twining phenomenon of high polymers in the transformation zone of the crack tip.

3.6. Exploring cross-sectional appearance and fracture regime

The pre-determined condition of fracture in organic glass is deformation of silver grains [9, 10, 12]. Based on observation with an optical microscope of the cross-section appearance of the slow [crack] extension zone, we can acknowledge the following: when the factor of the stress intensity at the crack tip reaches K_{1c}, the molecular chains in coarse filaments (Fig. 5) of the silver grain structure are under excessive stress, thus breaking the main chains. Moreover, terminals of molecules or molecular chains of low molecular weight easily slip out by the action of tensile stress. Plasticizers in two types of organic glass intensify this slipping phenomenon. Thus, filament after filament of coarse filaments break and the crack begins slowly to extend. Moreover, new silver grains form at the crack tip. During the initial stage of crack extension, the molecules have sufficient time for orientation, thus producing slender necks, forming gradually into coarse filaments. Later, breaks occur at the central portion one after the other, forming orientation molecular layers at their cross section. Figure 7 (refer to plate no. 15 [not available in xerox copies of text]) shows cross sections of two types of glass. In the slow extension [of the crack] zone, a light reflection effect (rainbow stripes) can be seen, created by the orientation layers. Below 60°C, the thickness of the color layer remains almost unchanged [9]. The micro-structure of the crack shown in Fig. 5 can better explain this phenomenon. The fracture mode of PMMA changes with higher cracking speeds. During low-speed extension of the crack, silver grains transform in single-plane fashion, from a change in higher speed to transformation to a multi-plane [17]. The mirror-surface zone of two types of organic glass is very small (Fig. 7). It is possible that all glass contains plasticizer; thus, silver grains easily transform into multi-faces. From Figs. 7 and 8 (refer to plate no. 15 [not available in xerox copies of text]), we can see very obvious boundaries between slow extension and fast fracture. At places close to the fast fracture zone, river-shaped or feather-shaped stripes can be seen. This can prove that the fracture process skips from one face of silver grains to another. Concerning the fracture process of the fast fracture zone of PMMA, there are quite a number of researchers [9, 18, 19]. No further discussion will be made in this paper.

IV. Conclusion

1. Starting from the basic viewpoint of fracture mechanics, by combining the inherent molecular motion and cross-section appearance of high polymer materials, it should be defined that the stress-intensity factor during crack initiation in a vitreous polymer is fracture toughness K_{1c} of plain strain; the stress-intensity factor during transition from a slow to fast crack [extension] speed is K (instability), which indicates the general situation of molecular motion of different polymers.

2. Based on the principle of equal-effectiveness of softness, two formulas for calculating equal-effectiveness crack length can be derived:

$$a = \frac{2}{3} a_3 + \frac{1}{6} (a_1 + a_5)$$

$$a = \frac{7}{90} (a_1 + a_5) + \frac{16}{45} (a_2 + a_4) + \frac{2}{15} a_3$$

3. At room temperature, fracture toughness of YB-4 glass is not much different from that of YB-3 glass. However, in the former case the K (instability) value is considerably smaller. This is possibly because large molecules have a high-polarity carboxyl group with greater rigidity and lower mobility.

4. There is no apparent effect on K_{1c} and K (instability) due to absorbing a small amount of water in the glass. After humid heating and ageing, the fracture properties of two types of glass are lower; this is related to a deficiency formed at the surface of test specimens.

Colleagues Zhao Jin, Ju Xiaoman and Zhang Xichang assisted in photographing cross sections of fracture faces; Lin Ronghuo, Wang Songzhi and Chai Xingguo assisted in measuring fracture toughness. The authors thank the aforementioned colleagues.

LITERATURE

[1] Key, P.I., NASA N68-29464, 1968.

[2] USAF MIL-P-25690A, 1960.

[3] Marshall, G.P., Williams, J.G., J.Mater. Sci., 8(1973), 138.

[4] Marshall, G.P., J.Mater. Sci., 9(1974), 1409.

[5] Margolis, R.D., ASTM STP601, 1976, 391-408.

[6] ANSI/ASTM E399-78, 1978.

[7] Hiroshi Tata, Paris,P.C., Irwin,G.R.,The Stress Analysis of Crack Handbook, Hellertown, Pa., Del Research Corporation, 1973.

[8] BS 5447-1977, 1977.

[9] Broutman, L.J., AD-736859, 1971, P.5-9, 15, 165, 168-170.

10. Li Hao et al, Duanlie Lixue [Fracture Mechanics], Shandong Science and Technology Publishing House, 1980, pp. 41.42.

[11] Hull, D., Deformation and Fracture of High Polymers, H.H.Kausch,Ed., Plenum Press, New York-London, 1972, 172.

[12] Hull, D., The Mechanics and Physics of Fracture, Churchill College, Cambridge,1975,13/1-13/7.

[13] Beaument, W.R., J.Mater. Sci., 10(1975), 1334.

[14] Williams, J.G., Pure Appl. Chem., 39(1974), 275.

[15] Gilbert, A.S., J.Appl. Polym. Sci., 21(1977), 319.

16. High Polymer Chemistry Faculty Research Laboratory, Beijing University, Preliminary Research Summary on Ageing Prevention of No. 4 Glass, Internal Use Only Information, 1970.

[17] Green, A.K., J. Mater. Sci., 11(1976), 577.

[18] Kusy, R.P., Turner, D.T., Polymer, 18(1977), 391.

19. Lu Xici, Gaofenzi Tongxun [High Polymer Communication], 4 (1981), 414.

STUDY OF UNIAXIAL COMPRESSIVE STABILITY OF CARBON FIBER COMPOSITE STIFFENED PLATES

Qin Renzhi, Shen Sitang and Wang Zhenming

Qin of Nanjing Institute of Aeronautics and Astronautics; Wang of Institute of Mechanics, Chinese Academy of Sciences

By means of the finite element methods, the numerical solutions of the integral and the local critical buckling stresses of the stiffened plates of carbon fiber composite are found. Three test specimens of longitudinal stiffened plates made from carbon fiber composite are subjected to uniaxial compressive stability test under the condition of simple supported on the sides, the critical buckling stresses thus determined show in better agreement with the numerical results calculated from finite-element methods.

I. Foreword

There is a series of outstanding characteristics of advanced carbon fiber composite material, namely its high specific strength and specific rigidity, as well as its good resistance against fatigue; composite material has been more and more emphasized by astronautical and aeronautical circles in developing research along multiple routes. It is contemplated to use carbon fiber composite material in making stiffened wall plates for the vertical fin of China's interceptor planes, thus considerably reducing the weight, enhancing flight mobility and flexibility, raising flight speed, and enhancing flight capability. At

present, the price of carbon fiber composite material is relatively expensive. In order to select materials rationally and to provide the basis for design of the aircraft structure, the authors studied the stability of composite stiffened plates under axial pressure; axial pressure tests were conducted using simple supported (at the sides) stiffened plates. The test results are relatively close to the critical stress of an unstable level plate calculated by using two calculation methods of limited elements.

II. Study on Tests of Axial Pressure Stability

Under the same technical conditions, three pieces of longitudinal stiffened composite material were made into test specimens. With the condition of simple support at the sides, axial pressure stability tests were made to observe the phenomenon of instability.

2.1. Test specimens and experimental methods

Figure 1 shows the geometric dimensions of the face plate and angle bar (iron).

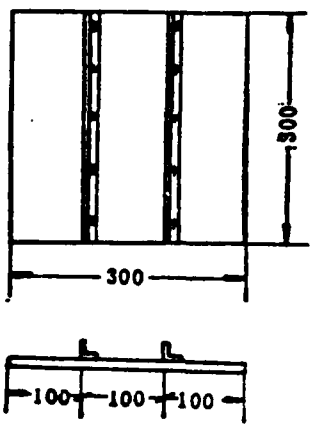

Fig. 1. Test specimen.

Face plate (square plate): 300x300x2.2 mm; angle iron (equal legs): 10x10 mm with 1.8 mm thickness.

The layer depositing method of the face plate and the angle bar (iron) is the same: $[0°/45°/0°/--45°/0°/90°]_s$; the thickness of the test specimen is the average thickness, taking the average value of thicknesses at nine points in the test specimen. The raw materials of the test specimens are Japanese-made Tori [Japanese transliteration] T-300 carbon fiber and Chinese-made epoxy resin (GP648, made by the Shanghai Resin Plant). In processing, first long carbon fibers are soaked in epoxy resin gel and then these fibers are laid into weftless cloth before dried. After the layers are laid at different angles, cutting is done. Then the material is placed into a thermal pressure can for solidification and forming. The wall plate and angle bars are then glued and connected with screws to prevent splitting. Then the piece is machined into the predetermined dimensions.

(1) Boundary conditions: In order to realize the boundary condition of simple support on the sides, a design using a V-shaped channel for the upper and lower loading sides, and knife-edge support at the lateral side is adopted. After two terminals of the longitudinal bar of the test specimen are reversed to an acute angle smaller than 40°, the test specimen is placed into the V-shaped channel as shown in Figs. 2 and 3.

The adjusting screw at the lateral side of the knife edge should not be turned too tight (generally, it is appropriate just to tighten by hand). The vertical column fixing the lateral side of the knife edge is a thick steel plate with relatively high rigidity.

The fixture was designed by the authors. As judging from the test result, the fixture has desirable characteristics.

(2) Test equipment and measurement method; Tests were conducted on a 100-ton material test device made by the Changchun Material Test Equipment Plant (Fig. 4, refer to plate no. 15 [not available in xerox copies of text]). By slowly turning an oil valve, quasi-static loading is attained. Three 100-division displacement transmitters were installed; two of the transmitters measured the axial-direction shortening; the other one measured the central deflection of the test specimen. Each transmitter was connected to an "X-Y" recording instrument.

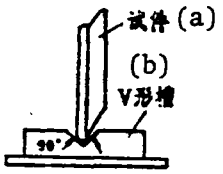

Fig. 2. Test specimen after reversing the angle of V-shaped channel and angle bar.
Key: (a) Test specimen; (b) V-shaped channel.

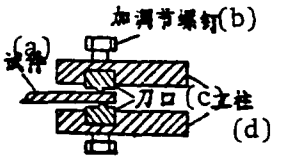

Fig. 3. Schematic diagram showing lateral side with addition of support.
Key: (a) Test specimen; (b) Addition of adjustment screw; (c) Knife edge; (d) Vertical column.

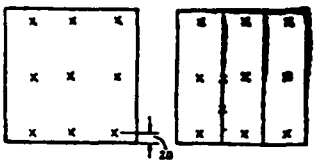

Fig. 5. Schematic diagram showing positions of strain sheets.

On the test specimen, 20-sheet paper electric resistance strain sheets are pasted to measure the strain (Fig. 5). The strain sheets pasted in the vicinity of upper and lower terminals of the test specimen are used to observe whether or not the loading is even and whether or not there is a terminal bending moment.

The schematic diagram of the measurement system is shown in the following:

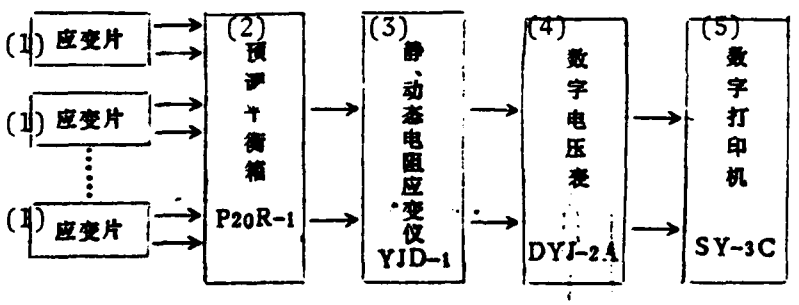

Key: (1) Strain sheet; (2) Pre-adjusted equilibrium box; (3) Static-dynamic electric resistance strain instrument; (4) Digital potentiometer; (5) Digital printer.

The schematic diagram for the recording system (loading--axial direction shortening curve, and loading--lateral deflection curve) is shown as follows:

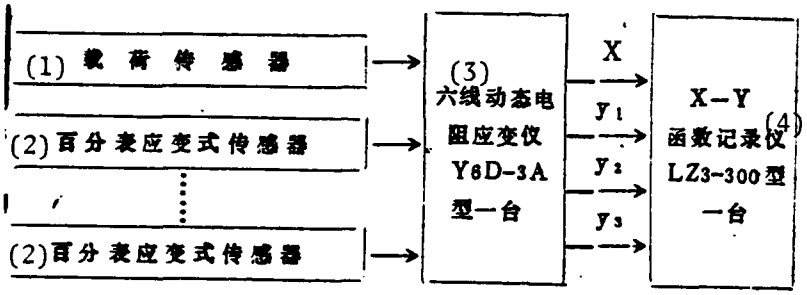

Key: (1) Load transmitter; (2) 100-division meter strain type transmitter; (3) Six-wire dynamic electric resistance strain instrument, one set; (4) X-Y function recording instrument model LZ3-300, one set.

2.2. Analysis of test phenomenon

At this time since the angle bar of the test specimen is designed to be relatively weak and short, there is no whole-body instability because of local instability, but only the instability of the whole body occurring independently.

At the beginning the load-deflection curve is nonlinear; this is because of the effect of the initial deflection and reverse angle at the angle iron portion (Fig. 6).

The load-axial-direction shortening curve (Fig. 7) is a broken line composed of two straight-line sectors; however, the mean load strain curve is close to linearity; refer to Figs. 8 and 9. When attaining the critical load, we can see from the load-strain and load-deflection curves that deformation and deflection increase quickly (or turn from increase into decrease). In particular, the load-axial-direction shortening curve is linear at small than 1700 kg load. Once the load is as high as 1700 kg, the curve deflects with a smaller inclination. This indicates that the axial-direction rigidity of the test specimen lowers significantly; in other words, both the effective width and loading capacity are lowered. Therefore, the critical load of test specimen I is 1700 kg.

After the test specimen attains the critical load, the specimen still has continuously increasing bearing capacity, which is static super-critical deformation. Continuous increase of loading can be applied to the test specimen.

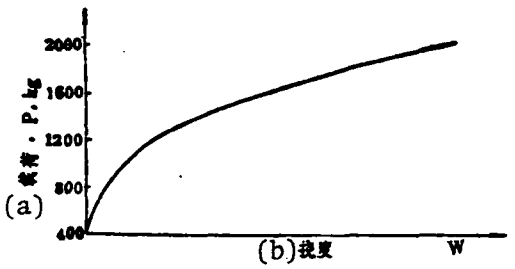

Fig. 6. Load (P)--deflection (W) curve, test specimen I.
Key: (a) Load; (b) Deflection.

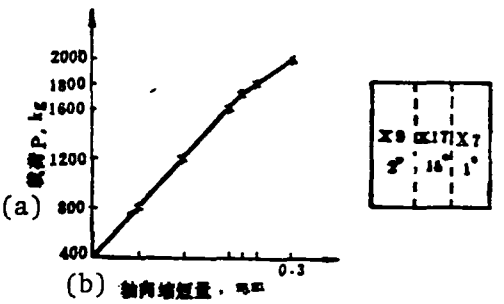

Fig. 7. Load (P)--axial direction shortening (Δ) curve.
Key: (a) Load; (b) Axial-direction shortening.

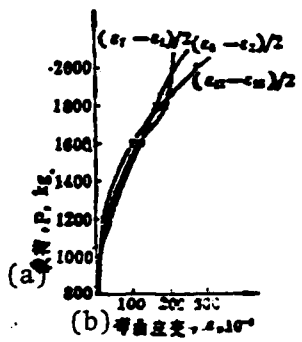

Fig. 8. Load (P)--bending strain curve, test specimen I.
Key: (a) Load; (b) Bending strain.

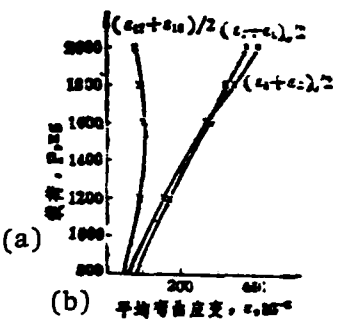

Fig. 9. Load (P)--mean strain curve, test specimen I.
Key: (a) Load; (b) Mean bending strain.

In addition, the authors conducted a rigid-support (at four sides) test, utilizing the test specimen after applying axial pressure with simple support at the sides. In the test method, the reverse bar angle portion of the specimen is cut off; the loading terminal of the specimen is fixed by a 5-mm level iron sheet, and the lateral side of the specimen is fixed by a 10-mm wide, level iron sheet (Fig. 10).

Fig. 10. Schematic diagram of loading terminal and tne lateral side of the fixture.
Key: (*) Test specimen.

Comparison between test value and value of limited element is as follows:

Rigid support test value (kg/cm^2) at the sides----------530.0;
Rigid support (at the sides) value from solution of limited elements----------809.8; and
Ratio----------65.4 percent.

The difference of two values [value from test result, and the calculated value] is as high as 34 percent. Upon analysis of the cause of the difference in the two values, first at the loading side, the rigid support condition has not been well realized. Besides, the test specimen has undergone the stability test of axial pressure with simple support at the sides, so the specimen is deformed quite a bit with more defects; this is an important reason in the lowered quality of the test specimen. Even under this condition, the critical stress (530 kg/cm^2) of stiffened plates close to the condition of rigid support is also significantly greater than the critical stress (241 kg/cm^2 as the average value) of stiffened plates with simple support at the sides. This indicates that the critical load can be significantly increased when rotation is restrained in the boundary conditions. In structural design, this point should be utilized as much as possible.

When the portion of the reverse angle iron of the test specimen is cut off, dimensions of the remaining specimen are: 300x270x2.2 mm. The purpose of the second test is to observe the damage phenomenon of instability. When the test specimen is unstable, bending deformation increases rapidly. At 5180 kg

of load, a loud "clap" sound occurred, indicating the start of splitting between layers. At 5600 kg of load, the sound continued in an on-and-off fashion. At 6050 kg of load, it became a continuous sound. Until the load at 6270 kg, a loud cracking sound occurred; a big split occurred between the bar and face plate of the loading terminal. This sound is produced due to excessive interlayer stress, causing interlayer splitting. At 6270 kg of load, the test specimen lost all its bearing capacity. In the case of aluminum test specimens, bearing capacity is lost following serious plastic deformation.

In order to compare critical stresses (loss of stability due to axial pressure) of aluminum test specimens of the same dimensions, useful experience can be gained. Before conducting tests on carbon fiber composite materials, first tests on aluminum specimens were conducted.

III. Results and Discussion

Three axial-pressure tests (with the same parameters) were conducted on stiffened plates with simple support at the sides. The test data were close together, indicating relatively good quality of the test specimen. Strict control of technical quality is the necessary condition to ensure low divergence of data.

1. Effect on critical stress by layer depositing methods in calculation of limited elements

In order to estimate the effect of deposited layers, three different methods of layer deposition were designed with thickness of 2.2 mm and the number of layer is 12.

A: $[\pm 45°/\pm 45°/\pm 45°]_s$
B: $[0°/0°/90°/0°/0°/90°]_s$
C: $[0°/45°/0°/-45°/0°/90°]_s$

It is assumed that various parameters of the bar are constant; it is further assumed that the critical stresses with limited-element calculation are, respectively, $\sigma_{cr}(A)$, $\sigma_{cr}(B)$, and $\sigma_{cr}(C)$. Then the calculation results are as follows:

	σ_{cr}公斤/厘米^2 (1)	$\sigma_{cr}(A),\sigma_{cr}(B)/\sigma_{cr}(C)$	$\sigma_{cr}(A),\sigma_{r}(C)/\sigma_{cr}$ (B)
(2)筋板A	309.0	109.4%	111.2%
(2)筋板B	278.0	98.4%	
(2)筋板C	282.4		101.6%

Key: (1) Kg/cm^2; (2) Stiffened plate.

As revealed by the aforementioned data, the calculated critical stress can differ by 11.2 percent whether or not the layer deposition is appropriate. In order to sufficiently utilize properties of composite material, during its optimizing design, appropriate design of layer deposition can be adopted to raise the critical stress.

2. It is assumed that the method of layer deposition of the face plate is still in three forms (A, B and C), and parameters of stiffened bars have remained constant. The following shows the comparison of calculated results with anisotropic (limited elements) calculation, and perpendicular intersection anisotropic (limited elements) calculation.

Stiffened plate:

	(a) 各向异性有限元解	正交各向异性有限元解 (b)	(d) 比值, %
(c) 筋板A	309	320.9	96.3
(c) 筋板B	278	278	100
(c) 筋板C	282.4	291.6	96.8

Key: (a) Solution from anisotropic (limited elements) calculation; (b) Solution from anisotropic (limited elements) calculation; (c) Stiffened plate; (d) Ratio value.

As revealed by the above data, the error in critical stress in two calculations of limited element is around 4 percent. The stiffened plate B is laid (in layers) at 0° and 90°; there are no bending rigidities D_{16} and D_{26}. Therefore, two solutions of limited elements are the same.

Level plate:

	(a) 各向异性有限元解	正交各向异性(b有限元解	比值, % (c)
(d) 平板A	105	117	89.7
(d) 平板C	76.7	86.5	88.7
$\sigma_{cr}(A)/\sigma_{cr}(C)$	136.9%	135.3%	

Key: (a) Anisotropic (limited elements) solution; (b) Perpendicular intersection anisotropic (limited elements) solution; (c) Ratio value; (d) Level plate.

We know from the aforementioned that the error is about 11 percent for level plates with different methods of calculation; however, for stiffened plates, the error is only 4 percent. The existence of the stiffened angle bar considerably enhances the longitudinal rigidity, relatively reducing the error effect because of neglecting D_{16} and D_{26}. The authors can also consider that appropriate deposition of layers can raise the calculated critical stress (of the level plate) by about 35 percent. For level plates, the effect of layer deposition is more pronounced.

3. The authors refer to Przemieniecki's structural analysis of local instability with limited elements, and Zienkiewicz et al. on structure and limited element method in continuous-medium mechanics; they calculated separately the critical stresses of instability of the level plate. Results are close.

	Zienkiewicz法 (a)	Przemieniecki法(a)
(b) 板A	86.5	89.1
(b) 板B	117	120

Key: (a) Method; (b) Plate.

We have to point out here that the number of elements by using Przemieniecki's method is considerably smaller than the number of elements by using Zienkiewicz's method. Thus, the number of elements stored can be reduced; time and expenses can be saved. However, various boundary conditions can be conveniently adapted by using Zienkiewicz's method; the calculated values are quite close to the test values. Therefore, the calculation of stiffened plates of carbon fiber composite material using Zienkiewicz's method is appropriate.

The authors measured, separately, the critical stresses (241.2 and 245.9 kg/cm^2) of composite material stiffened plates and aluminum stiffened plates; the critical stresses of instability are almost the same (the critical load for an aluminum stiffened plate is 1800 kg). For carbon fiber composite material, the stress distribution situation can be utilized to design layer deposition; this can sufficiently exploit the superior anisotropy of this material.

The authors thank Wang Zhenjiang of Institute of Mechanics, Chinese Academy of Sciences, and Yu Dechang of Beijing Aeronautical Material Research Institute for their assistance.

LITERATURE

[1] Timoshenko,S.P. and Gere,J.M., Theory of Elastic Stability 2nd ed.,McGraw-Hill Book Co., N.Y.1961.

[2] Jones, R.M., Mechanics of Composite Materials., 1975.

3. Tsai, S. W., Introduction to Mechanics of Composite Material (Chinese translation), Science and Technology Information Institute, Third Ministry of Machine Building, 1981.

4. Holand, I. and Bell, K., Application of Limited Element Method in Stress Analysis (Chinese translation), Science Publishing House, 1978.

[5] Ashton J.E. and Love, T.S., "Experimental Study of the Stability of Composite Plates" , J. of Composite Materials,1969,p.230.

[6] Jones,R.M.,Buckling of Circular Cylindrical Shells with Multiple Orthotropic Layers and Eccentric Stiffeners" ,AIAA Journal,Dec.1968,P.2301.

[7] Przemieniecki J.S.,Finite Element Structural Analysis of Local Instability, AIAA Journal, 11(1973), No.1.

8. Zienkiewicz, O. C. and Cheung, Y. K., Structure and Limited Element Method in Continuous Medium Mechanics (Chinese translation), National Defense Industry Publishing House, 1975.

END

FILMED

5-84

DTIC